



Modeling the Strongest Silicate Emission Features of Local Type 1 AGNs

M. Martínez-Paredes¹, O. González-Martín², D. Esparza-Arredondo², M. Kim¹, A. Alonso-Herrero³, Y. Krongold⁴,
T. Hoang¹, C. Ramos Almeida^{5,6}, I. Aretxaga⁷, D. Dultzin⁴, and J. Hodgson¹

¹ Korea Astronomy and Space Science Institute 776, Daedeokdae-ro, Yuseong-gu, Daejeon, Republic of Korea (34055); mariellauriga@kasi.re.kr

² Instituto de Radioastronomía y Astrofísica UNAM Apartado Postal 3-72 (Xangari), 58089 Morelia, Michoacán, Mexico

³ Centro de Astrobiología, CSIC-INTA, ESAC Campus, E-28692 Villanueva de la Cañada, Madrid, Spain

⁴ Instituto de Astronomía UNAM, México, CDMX., C.P. 04510, Mexico

⁵ Instituto de Astrofísica de Canarias (IAC), E-38205 La Laguna, Tenerife, Spain

⁶ Departamento de Astrofísica, Universidad de La Laguna (ULL), E-38206 La Laguna, Tenerife, Spain

⁷ Instituto Nacional de Astrofísica, Óptica y Electrónica (INAOE), Luis Enrique Erro 1, Sta. Ma. Tonantzintla, Puebla, Mexico

Received 2019 October 14; revised 2019 December 20; accepted 2019 December 28; published 2020 February 24

Abstract

We measure the 10 and 18 μm silicate features in a sample of 67 local ($z < 0.1$) type 1 active galactic nuclei (AGN) with available *Spitzer* spectra dominated by nonstellar processes. We find that the 10 μm silicate feature peaks at $10.3_{-0.9}^{+0.7} \mu\text{m}$ with a strength ($\text{Si}_p = \ln f_p(\text{spectrum})/f_p(\text{continuum})$) of $0.11_{-0.36}^{+0.15}$, while the 18 μm one peaks at $17.3_{-0.7}^{+0.4} \mu\text{m}$ with a strength of $0.14_{-0.06}^{+0.06}$. We select from this sample sources with the strongest 10 μm silicate strength ($\sigma_{\text{Si}_{10\mu\text{m}}} > 0.28$, 10 objects). We carry out a detailed modeling of the infrared spectrometer/*Spitzer* spectra by comparing several models that assume different geometries and dust composition: a smooth torus model, two clumpy torus models, a two-phase medium torus model, and a disk+outflow clumpy model. We find that the silicate features are well modeled by the clumpy model of Nenkova et al., and among all models, those including outflows and complex dust composition are the best. We note that even in AGN-dominated galaxies, it is usually necessary to add stellar contributions to reproduce the emission at the shortest wavelengths.

Unified Astronomy Thesaurus concepts: Active galactic nuclei (16); Infrared astronomy (786); Dust continuum emission (412); Active galaxies (17)

1. Introduction

A dusty torus surrounds the central engine of active galactic nuclei (AGNs) on a scale of a few pc (e.g., Krolik & Begelman 1988; Antonucci 1993; Robson et al. 1995; Peterson 1997). It shines at infrared (IR) wavelengths between 1 and 1000 μm peaking at around 20 μm (e.g., Sanders et al. 1989; Elvis et al. 1994). This emission is the result of the IR re-radiation of optical-UV light generated around the central black hole (BH) that has been absorbed by the dusty torus (Neugebauer et al. 1979). The main observational components that describe it are the slope of the spectral energy distribution (SED) between 1 and 8 μm , and the strength of the silicate features around 10 μm and 18 μm that are produced within the warm dust of the torus that the AGN directly illuminates. The silicate features have been observed mostly in emission with the mid-infrared (MIR) infrared spectrometer (IRS) *Spitzer* in type 1 AGN (Hao et al. 2005; Siebenmorgen et al. 2005; Hatziminaoglou et al. 2015). In these AGNs, the 10 μm silicate feature is broader and peaks at much longer wavelengths (~ 10.0 – $11.5 \mu\text{m}$) than the “normal” silicate emission feature of the Galactic interstellar medium (ISM; e.g., Hao et al. 2005; Siebenmorgen et al. 2005; Sturm et al. 2005; Li et al. 2008). This suggests different silicate compositions, such as a different proportion and/or size of grains (e.g., Shi et al. 2006; Li et al. 2008; Xie et al. 2017).

Martínez-Paredes et al. (2017) used the starburst-subtracted IRS/*Spitzer* spectra of 20 quasi stellar objects (QSOs) between ~ 7.5 and 15 μm plus the unresolved near-infrared (NIR) emission to constrain the parameters of the dusty torus using the CLUMPY models of Nenkova et al. (2008a, 2008b). They noted that in most cases, the spectral range around 8 μm is underestimated by the CLUMPY models and that trying to fit

this part of the spectrum resulted in a bad fit of the silicate feature at 10 μm . Furthermore, in most cases, the peak of the 10 μm silicate feature was shifted from the model location.

Considering that the shape and peak of the silicate features are strongly correlated with the properties of the dust (e.g., Draine et al. 2007; Sirocky et al. 2008), in this work, we use five of the most popular torus models to investigate how well they reproduce the strongest silicate emission features observed in type 1 AGNs. Recently, González-Martín et al. (2019a) compared these models and found that they can be distinguished according to the continuum slopes and silicate strengths, and in a second work (González-Martín et al. 2019b), they used MIR spectroscopy data of type 1 and type 2 AGNs in the *Swift*/BAT survey to investigate how these models reproduce their spectral continuum. We focus our study on type 1 AGNs with strong silicate emission features because: (1) for type 2 AGNs, the inclusion of a fraction ($\sim 50\%$) of silicate grains, either based on Draine (2003) or Ossenkopf et al. (1992), are enough to reproduce the observed silicate features in absorption (see, e.g., Alonso-Herrero et al. 2011; Ramos Almeida et al. 2011; Martínez-Paredes et al. 2015); and (2) the silicate features are well above the continuum in the low-resolution *Spitzer* spectra, which support the interpretation that the silicate features are due to AGN activity.

In this paper, we aim at exploring how accurately smooth, clumpy, two-phase, and outflow torus models reproduce the IRS/*Spitzer* spectra of these objects, and analyzing the results in terms of physical differences like the geometry and dust composition assumed. The first model that we consider is the smooth torus model of Fritz et al. (2006, Fritz06 hereafter), which assumes a continuous distribution of dust composed of graphite and silicate grains in almost equal percentages. The second model is the CLUMPY torus model of Nenkova et al. (2008a, 2008b,

Nenkova08), which assumes a standard ISM dust composition of 53% silicates and 47% graphite with sizes between 0.025 and 0.25 μm . The third torus model is clumpy (Hönig & Kishimoto 2010, Hoening10) and assumes three dust components that include the standard ISM composition, the standard ISM composition with larger grains (0.1–1.0 μm), and a larger fraction of graphite grains (30% silicates and 70% graphite, with sizes between 0.05 and 0.25 μm). The fourth model (Hönig & Kishimoto 2017, Hoening17) has two components: a dusty clumpy disk that takes into account the emission from the hotter dust close to the central engine; and a hollow cone formed by a wind of clumpy dusty clouds elongated toward the polar direction. This model assumes that the wind is originated close to the sublimation zone of the dusty disk. Because of that, the dust in the wind has similar properties to the dust in the sublimation zone.

The paper is organized as follows: In Section 2, we present our sample selection and data. In Section 3, we describe the models, while in Section 4, we present the analysis. In Section 5, we present the discussion, and our summary and conclusions are presented in Section 6. We adopt the following cosmology: $H_0 = 73 \text{ km s}^{-1} \text{ Mpc}^{-1}$, $\Omega_M = 0.30$ and $\Omega_\Lambda = 0.70$.

2. The Sample and Data

2.1. The Silicate-dominated Local AGN

We use the latest version of the AGN catalog of Véron-Cetty & Véron (2010) and the sample of low-luminosity type 1 AGN in Mason et al. (2012) to select AGN that have redshifts $z < 0.1$ and available 2D low-resolution IRS/*Spitzer* spectra in the CASSIS database (v6., Lebouteiller et al. 2011). We select those objects with spectra extracted as point-sources that cover the 5–35 μm spectral range. The first criterion allows us to probe the MIR emission from the central region of the AGN, and the second one allows us to study both the 10 and 18 μm silicate features. As an exception, we include NGC 3998, a strong silicate emitter (e.g., Mason et al. 2012), which has a low-resolution spectrum in the ~ 7.5 –14.5 μm range and a high-resolution spectrum in the ~ 14 –35 μm range. In order to ensure that the emission in the IRS/*Spitzer* spectra is mostly dominated by dust heated by the AGN, we decompose them into their stellar, ISM, and AGN emission (dust heated by AGN) components at ~ 5 –15 μm , using the spectral decomposition tool DEBLENDIRS (Hernán-Caballero et al. 2015). For more details on the spectral decomposition, we refer the reader to Appendix A. We select only those objects (67) for which the spectral contribution due to AGNs is $> 80\%$ (see Figure 1). Hereafter, we refer to the spectra of these objects as the AGN-dominated IRS/*Spitzer* spectra. Note that we refer here to the original spectra, not to the component obtained from the decomposition.

2.2. The IRS/*Spitzer* Spectra

We obtained the reduced low-resolution ($R \sim 60$ –127) IRS/*Spitzer* spectra from the CASSIS database (v6., Lebouteiller et al. 2011). The spectra include the SL1 ($\lambda \sim 7.4$ –14.5 μm) and SL2 ($\lambda \sim 5.2$ –7.7 μm) modules with a slit-width of $3''6$, and the LL1 ($\lambda \sim 19.9$ –39.9 μm) and LL2 ($\lambda \sim 13.9$ –21.3 μm) modules with a slit-width of $10''5$ (Houck et al. 2004; Werner et al. 2004). We use the final stitched spectra between 5 and

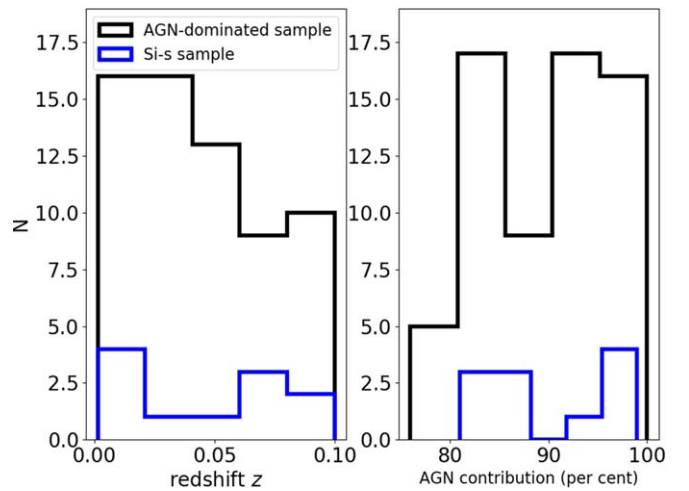


Figure 1. Properties of the sample. Left panel: distribution of redshifts. Right panel: distribution of AGN contributions to the IRS/*Spitzer* spectra. The black line represents the full sample, and the blue line is a subsample defined in Section 2.1.

35 μm . The different module spectra were stitched by scaling the LL and SL1 flux modules to the shortest module SL2 flux.

2.3. Measuring the Silicate Emission Features

To measure the silicate emission features, we start by interpolating a local continuum between both sides of the emission-line complexes. We inspect each spectrum visually and choose three bands in which to measure the continuum. Band 1 is located at the blue extreme of the 10 μm silicate feature, while band 3 is located at the red extreme of the 18 μm silicate feature, and band 2 is located between the two silicates. Bands 1, 2, and 3 are located within the 7.8–8.5, 13.5–14.0, and 20.0–21.0 μm ranges.

In order to better define uncertainties in the continuum definition, which might be affected by the presence of Polycyclic Aromatic Hydrocarbon (PAH) molecular emission lines around 7 μm , and in some cases by the artificial “teardrop”⁸ feature around 14 μm , we trace fiducial mean values of each continuum band by bootstrapping on the measured fluxes (hatched pink regions in Figure 2). We generate 100 continuum values, considering the uncertainties, between bands 1 and 2, and between bands 2 and 3. We randomly associate shorter and longer wavelength mean continuum values to generate linear continua below the silicate features. We note that fitting a spline continuum gives similar results. The dark blue solid lines in Figure 2 are bootstrapped local continua derived from the continuum bands and they define the regions where we measure the strength of the silicate features.

Considering that the peak of the silicate features vary from object to object, we choose to measure the strength of the features at the wavelengths where they peak. However, for simplicity, we still call them the 10 and 18 μm silicate features. The silicate strength is, hence, defined as the silicate peak relative to the continuum, at the wavelength where the silicate feature peaks (see, e.g., Hao et al. 2007), according to the

⁸ An excess of emission present in the 2D SL1 spectrum of some objects.

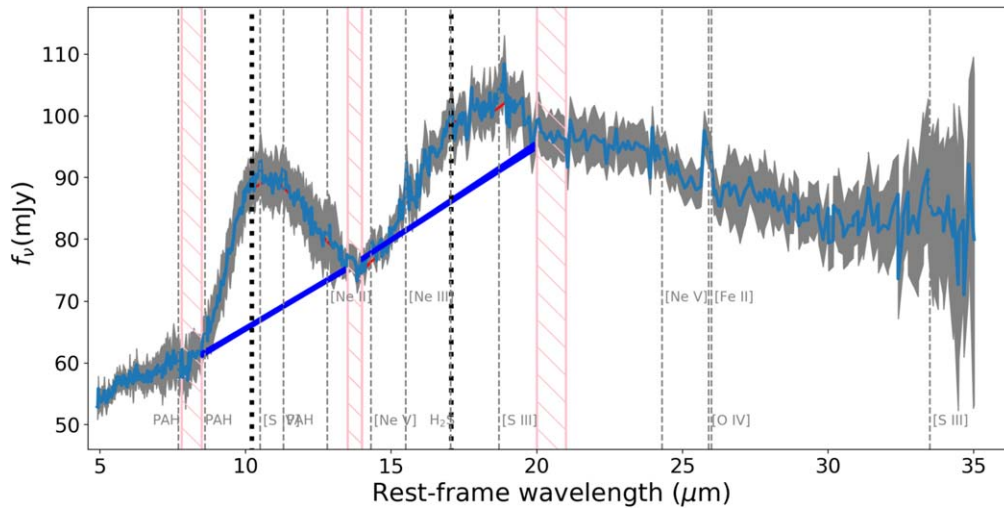


Figure 2. IRS/*Spitzer* spectrum of PG 2214+139 (light blue solid line). The red line is the local continuum that follows the broad features of the IRS/*Spitzer* spectrum. The blue solid lines are the bootstrapped local continua, and the vertical pink dashed bars are the bands used to fit the continua around the features. The vertical black dashed lines indicate the wavelength where the silicate strength is measured. The vertical gray dashed lines mark other emission lines.

Table 1
Basic Properties of Objects in the Si-s Sample and Their Silicate Feature Strengths Measured from the IRS/*Spitzer* Spectra

Name	Activity ^a	z	$\log L_{X(2-10\text{keV})}$ erg s ⁻¹	Ref.	λ_p (μm)	$\text{Si}_{10\mu\text{m}}$	λ_p (μm)	$\text{Si}_{18\mu\text{m}}$
NGC 7213	LINER	0.0058	42.2	6	10.7 ± 0.1	0.52 ± 0.05	17.3 ± 0.1	0.23 ± 0.04
PG 2304+042	Sy1.2	0.0420	43.4*	9	10.3 ± 0.1	0.30 ± 0.06	17.3 ± 0.1	0.33 ± 0.08
PKS 0518-45	LINER	0.0420	44.9	8	10.4 ± 0.2	0.31 ± 0.05	17.6 ± 0.1	0.18 ± 0.04
PG 0844+349	Sy1/QSO	0.0640	43.7	1	10.3 ± 0.1	0.33 ± 0.06	16.7 ± 0.1	0.18 ± 0.04
PG 1351+640	Sy1.5/QSO	0.0882	43.1	6	9.8 ± 0.1	0.52 ± 0.03	18.4 ± 0.1	0.14 ± 0.03
PG 2214+139	Sy1.0/QSO	0.0658	43.8	1	10.2 ± 0.1	0.29 ± 0.04	17.8 ± 0.2	0.14 ± 0.04
PG 0804+761	Sy1/QSO	0.1000	44.5	1	9.9 ± 0.1	0.36 ± 0.03	17.3 ± 0.1	0.11 ± 0.04
OQ208	Sy1.5	0.0766	40.8	3	10.2 ± 0.1	0.34 ± 0.05	16.5 ± 0.1	0.12 ± 0.04
NGC 4258	LINER ^b	0.0015	40.9	5	11.0 ± 0.1	0.29 ± 0.05	17.3 ± 0.1	0.17 ± 0.04
NGC 3998	LINER	0.0035	41.2	4	10.7 ± 0.1	0.36 ± 0.01	$16.3 \pm 0.1^*$	0.23 ± 0.02

Note. Columns 1 and 2 list the name and type of activity, column 3 gives the redshift, and columns 4 and 5 list the logarithm of the intrinsic hard X-ray luminosity and the corresponding reference, respectively. Columns 6 and 7 list the wavelength where the $10\mu\text{m}$ silicate emission feature peaks, and the $10\mu\text{m}$ silicate strength, and columns 8 and 9 are the wavelength and strength of the $18\mu\text{m}$ silicate emission feature, respectively. *This value needs to be used carefully, since we are using the high angular resolution spectrum to fix the band 3 and measure the $18\mu\text{m}$ silicate feature strength. References:^aNED and Véron-Cetty & Véron (2010), ^bMason et al. (2012). *Estimated from (15 to 150)+keV X-ray luminosity assuming a spectral power law with an index $\alpha = 1.8$. References for hard X-ray luminosity: 1: Zhou & Zhang (2010); 2: Sambruna et al. (2011); 3: Ueda et al. (2005); 4: Younes et al. (2011); 5: Cappi et al. (2006); 6: Bianchi et al. (2009); 7: Brightman & Nandra (2011); 8: Winter et al. (2012); 9: Tueller et al. (2010); 10: Cusumano et al. (2010).

equation:

$$\text{Si}_p = \ln \frac{f_p(\text{spectrum})}{f_p(\text{continuum})}. \quad (1)$$

In Table 1, we list the mean and the 68% intervals for the objects with the largest silicate feature strengths. In Appendix B, we list the silicate emission strengths for the full sample. On average, we find that type 1 AGN have a $10\mu\text{m}$ silicate strength $\text{Si}_{10.3\mu\text{m}} = 0.13_{-0.37}^{+0.15}$ that peaks at $10.3_{-0.9}^{+0.7}\mu\text{m}$, and a $18\mu\text{m}$ silicate strength $\text{Si}_{17.3\mu\text{m}} = 0.14_{-0.06}^{+0.06}$ that peaks at $17.3\mu\text{m}$.

In most cases, our measurements, which were performed using the AGN-dominated *Spitzer* spectra, produce similar results to previous works (Hao et al. 2005; Sirocky et al. 2008; Thompson et al. 2009; Mendoza-Castrejón et al. 2015) (see Appendix B). Additionally, we compare our measurements of the silicate strengths with the values obtained using

DEBLENDIRS and find that they are similar within the uncertainties (see Appendix A).

2.4. Sample Selection

We build our final sample by selecting only those objects that show the strongest silicate emission features (see Table 1). From the original sample of 67 local type 1 AGNs, we select those objects with the largest $10\mu\text{m}$ silicate strength ($\sigma_{\text{Si}_{10\mu\text{m}}} > 0.28$, see Figure 3). The final sample is composed of 10 objects: six Seyfert (Sy) galaxies, and four low-ionization nuclear emission-line region (LINER) galaxies. Four of the Seyfert galaxies are also classified as PG QSOs. Note that we are not selecting the sample according to the type of AGN. We list the type only to give information about their basic properties.

Hereafter, we will refer to this sample as the type 1 AGN strong Silicate selected sample (Si-s). The sample spans a

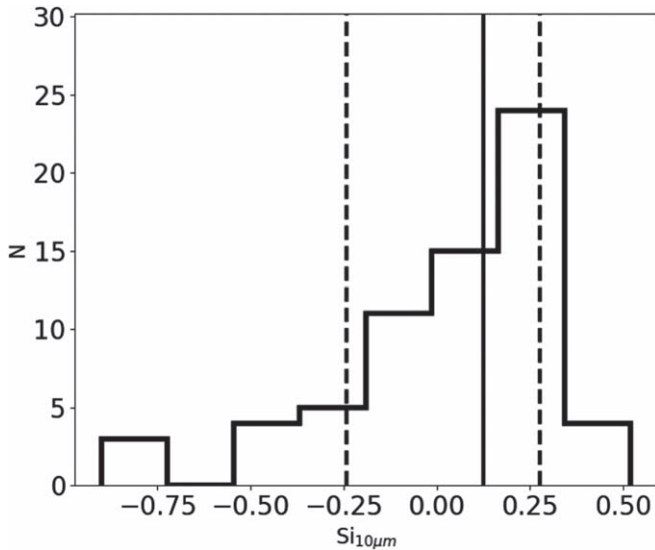


Figure 3. Distribution of the 10 μm silicate strength feature (see Table 1). The solid and dashed black lines indicate the mean and its 1σ confidence interval.

range of hard (2–10 keV) X-ray unobscured luminosities between $\sim 10^{41}$ and $\sim 10^{45}$ erg s^{-1} .

3. Dusty Torus Models

There are two types of torus models widely used in the literature: smooth torus models and clumpy torus models. Smooth models assume a continuous distribution of the dust in the torus (Pier & Krolik 1992; Efstathiou & Rowan-Robinson 1995; Granato et al. 1997; Fritz et al. 2006), while clumpy models assume a distribution of dusty clouds or clumps in a toroidal structure (Dullemond & van Bemmell 2005; Nenkova et al. 2008a, 2008b; Hönlig & Kishimoto 2010, 2017).

For simplicity, smooth models assumed a continuous distribution of the dust in the torus, so the temperature of the dust decreases monotonically with the distance from the central BH. According to this type of model, only type 1 AGNs produce 10 μm silicate features in emission and type 2 AGNs produce silicate features in absorption, implying an edge-on orientation with respect to the observer. In type 2 AGNs, therefore, the outer region of the torus hides the emission produced by the hotter and warmer dust in the inner part of the torus. However, the silicate depth that this model predicts is larger than observed in type 2 s, and it fails to explain silicate features in emission in type 2 QSOs (e.g., Sturm et al. 2006).

Conversely, clumpy models (e.g., Nenkova et al. 2008a, 2008b) never produce very deep absorption silicate features, and they predict silicate features in emission in type 1 and type 2 AGNs for a large combination of parameters (see, e.g., Nikutta et al. 2009). A third type of model combines clumpy and smooth properties to produce a two-phase medium dusty torus model (Stalevski et al. 2012, 2016). This model assumes a distribution of dusty clumps with constant and high density, embedded in a smooth dusty component of low density.

This was motivated by observational evidence that suggests that dust around AGNs seems to have a multiphase filamentary structure (Wada et al. 2009; Wada 2012).

A more recent model proposes a geometry composed by a compact and geometrically thin disk in the equatorial region plus an extended elongated polar structure of clumpy dust, that is copatial with the outflow of the AGNs (Hönlig &

Kishimoto 2017). This geometry is inferred from interferometric observations of nearby Seyfert galaxies, where the bulk of the MIR emission originates from the polar region rather than the equatorial plane (e.g., Raban et al. 2009; Hönlig et al. 2012, 2013; Tristram et al. 2014; López-Gonzaga & Jaffe 2016).

In this paper, we use the AGN-dominated IRS/*Spitzer* spectra of our Si-s sample of type 1 AGNs to investigate which models are able to better reproduce the peak and shape of the strongest silicate emission features observed. In the following subsections, we briefly describe the main geometrical and physical properties of the models, and Table 2 summarizes the different geometries and dust compositions assumed for each model.

3.1. Smooth Torus Model of Fritz et al. (2006)

This model is represented by a flared disk delimited by the inner and outer torus radius (e.g., Efstathiou & Rowan-Robinson 1995). The inner radius (R_{min}) is defined by the sublimation temperature of dust grains (1500 K) under the strong radiation produced by the central engine. The size of the torus is determined by the outer radius ($Y = R_{\text{out}}/R_{\text{in}}$, where Y is a free parameter), and the angular width of the torus Θ (see the cartoon (a) in Figure 4). This model assumes that the dust is composed of graphite grains (53%) with sizes from 0.005 to 0.25 μm , and silicate grains (47%) with sizes from 0.025 to 0.25 μm . The grain sizes are distributed according to Mathis et al. (1977). For the two species, they used the scattering and absorption coefficients given by Laor & Draine (1993). The dust is illuminated by an isotropic central point-like emitting source, which is represented by a broken power law of the form $\lambda L_{\lambda} \propto \lambda^{\alpha}$, with $\alpha = 1.2$ if $0.001 < \lambda < 0.03 \mu\text{m}$, $\alpha = 0$ if $0.03 < \lambda < 0.125 \mu\text{m}$, and $\alpha = 0.5$ if $0.125 < \lambda < 20.0 \mu\text{m}$. Other parameters of the model are the viewing angle i , the polar (γ) and radial (β) indices of the gas density distribution $\rho(r, \Theta) \propto r^{\beta} e^{-\gamma \times \cos(\Theta)}$ within the torus, and the optical depth $\tau_{9.7 \mu\text{m}}$. For a more complete description of this model, see Fritz et al. (2006).

3.2. Clumpy Torus Models of Nenkova et al. (2008a, 2008b)

This type of model assumes a central point-like emitting source surrounded by a toroidal distribution of clouds. The emission of the central source is characterized by a broken power law of the form $\lambda f_{\lambda} \propto \lambda^{1.2}$ for $\lambda \leq 0.01 \mu\text{m}$, $\propto \lambda^{-0.5}$ for $0.1 \mu\text{m} \leq \lambda \leq 1 \mu\text{m}$, $\propto \lambda^{-3}$ for $\lambda \geq 1 \mu\text{m}$, and a constant power law between 0.01 and 0.1 μm . Due to its clumpy nature, the central source can directly heat the dust in the inner region of the torus and the dust located at several sublimation radii from the central source. This model assumes standard Galactic spherical dust grains (standard ISM) composed of graphites (47%, Draine 2003) and silicates (53%, Ossenkopf et al. 1992), with a power-law distribution of grain sizes ($\propto a^{-3.5}$), where $a_{\text{min}} = 0.05\text{--}0.01 \mu\text{m}$ and $a_{\text{max}} = 0.25 \mu\text{m}$, respectively. This model has six free parameters: the viewing angle i , the number of clouds along the equatorial ray N_0 , the angular width σ , the radial extend $Y = R_{\text{outer}}/R_{\text{inner}}$, the index of the radial distribution of clouds q , and the optical depth per cloud τ_V (see cartoon (b) in Figure 4). For a more complete description of this model, see Nenkova et al. (2008a, 2008b).

Table 2
Dust Properties of the Models

Model Name	Geometry	Dust Composition	Scattering and Absorption Coefficients	Grain Sizes*(μm)	
				Graphites	Silicates
Fritz06	Smooth torus	Graphite and Silicates	graphite and silicates Laor & Draine (1993)	0.005–0.25	0.025–0.25
Nenkova08	Clumpy torus	Standard ISM	graphites, Draine (2003) silicates, Ossenkopf et al. (1992)	(0.005–0.01)–0.25	
Hoening10	Clumpy torus	Standard ISM +standard ISM with large grains +graphite dominated dust (70% graphite and 30% silicates)	graphites, Draine (2003) silicates, Draine (2003) Ossenkopf et al. (1992)	(0.005–0.01)–0.25	0.1–1.0 0.05–0.25
Hoening17	Disk+Outflow	Standard ISM +standard ISM with large grains	like Hoening10	(0.005–0.01)–0.25	
Stalevski16	Two-phase media torus	Graphite and Silicates	Laor & Draine (1993) Li & Draine (2001)	0.005–0.25	0.005–0.25

Note. Assuming the distribution from Mathis et al. (1977), usually called the MNR distribution, the composition of the standard ISM is 47% graphite and 53% silicates. The numbers inside the parenthesis indicate the minimal range of sizes for the smaller grains.

3.3. Clumpy Torus Models of Hönic & Kishimoto (2010)

In this case, the toroidal distribution of dusty clumps surrounds a central point-like emitting source, which is described by a broken power law of the form $\lambda f_\lambda \propto \lambda$ for $\lambda < 0.03 \mu\text{m}$, $\propto \lambda^{-3}$ for $\lambda > 3 \mu\text{m}$, constant for λ between 0.03 and $0.3 \mu\text{m}$, and $\propto \lambda^{-4/3}$ for λ between 0.3 and $3 \mu\text{m}$. They modeled the torus following a 3D Monte Carlo radiative transfer simulation. These kinds of simulations fail to properly sample optically thick surface regions with enough grid cells so that each cell is optically thin, which results in underestimating the emission temperature and resulting in a smaller number of model clouds with respect to Nenkova et al. (2008a, 2008b). The dust is composed of three components: a standard ISM component, a standard ISM component with larger grains ($a_{\text{min}} = 0.1 \mu\text{m}$ and $a_{\text{max}} = 1.0 \mu\text{m}$), and intermediate to larger grains ($a_{\text{min}} = 0.05 \mu\text{m}$ and $a_{\text{max}} = 0.25 \mu\text{m}$) with 70% graphite and 30% silicates. The free parameters that describe this model are the viewing angle i , the number of clouds along the equatorial ray N_0 , the half-opening angle Θ , the index of the radial distribution a , and the optical depth τ_V (see cartoon (b) in Figure 4). For a more complete description of this model, see Hönic & Kishimoto (2010).

3.4. Clumpy Disk+Outflow Models of Hönic & Kishimoto (2017)

This type of model is based on the parameterization of the clumpy torus model of Hönic & Kishimoto (2010), but instead of adding a blackbody component to take into account the NIR emission, they include a set of different sublimation temperatures for silicate and graphite dust that results in more emission from graphite located in the inner edge of the torus. In this way, when the dust is heated to temperatures $>1200 \text{ K}$, smaller silicate grains are destroyed leaving only graphite grains that can be heated up to 1900 K . In the innermost radius only, grains with a size between 0.075 and $1 \mu\text{m}$ survive.

The clouds are distributed according to a radial power law $\propto r^a$, where a is the power-law index and r the distance from the black hole in units of the sublimation radius r_{sub} . They also add a polar outflow, modeled as a hollow cone that can be characterized by the radial distribution of dust clouds in the wind a_w , the half-opening angle of the wind (Θ_w), and the angular width (σ_Θ). Other parameters are the number of clouds

along the equatorial ray N_0 , and the scale height in the vertical Gaussian distribution of clouds h in the disk, (see cartoon (c) in Figure 4). For a more complete description of this model, see Hönic & Kishimoto (2017).

3.5. Two-phase Medium Dusty Torus Models of Stalevski et al. (2016)

This kind of models assumes a distribution of high-density dusty clumps embedded in a low-density smooth dusty component. This assumption produces both weaker silicate features and a pronounced NIR emission. They assume that the accretion disk in the nucleus radiates as a broken power law of the form $\lambda L_\lambda \propto \lambda^\alpha$, where $\alpha = 1.2$ for a spectral range of $0.001 \leq \lambda \leq 0.01 \mu\text{m}$, $\alpha = 0$ for $0.01 < \lambda \leq 0.1 \mu\text{m}$, $\alpha = -0.5$ for $0.1 < \lambda \leq 5 \mu\text{m}$, and $\alpha = -3$ for $5 < \lambda \leq 50 \mu\text{m}$. The dust is distributed following a law that allows a density gradient along the radial (r) and polar (θ) directions, inside a flare disk defined by the inner (R_{in}), outer radii (R_{out}), and half-opening angle. The inner radius is defined by the sublimation temperature of 1500 K for an average dust grain size of $0.05 \mu\text{m}$. They assumed a standard ISM dust composition with optical properties from Laor & Draine (1993) and Li & Draine (2001). For a more complete description of this model, see Stalevski et al. (2012, 2016).

4. Analysis

4.1. Synthetic and Observed Silicate Peak Wavelengths and Strengths

In this section, we explore how well the dusty torus models reproduce the central wavelength and strength of both 10 and $18 \mu\text{m}$ silicate features, and the NIR (α_{NIR}) and MIR (α_{MIR}) spectral indexes. In order to make a proper comparison, the synthetic and observed central wavelength and strength of both the 10 and $18 \mu\text{m}$ silicate features are measured following the same methodology described in Section 2.3, and fixing the bands to the sides of the silicate features between 7 and $7.5 \mu\text{m}$, 14 – $15 \mu\text{m}$, and 25 – $26 \mu\text{m}$. The synthetic and observed spectral indexes α_{NIR} and α_{MIR} are measured between 5.5 and $7.5 \mu\text{m}$, and between 7.5 and $14.0 \mu\text{m}$, respectively, according to the following definition $\alpha_{2,1} = -\log(f_\nu(\lambda_2)/f_\nu(\lambda_1))/\log(\lambda_2/\lambda_1)$, with $\lambda_2 > \lambda_1$ (see, e.g., Buchanan et al. 2006).

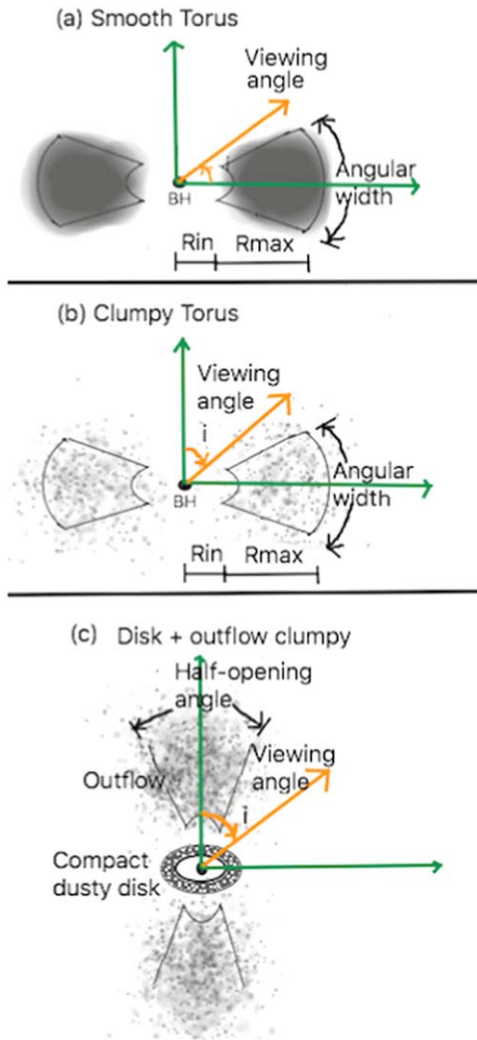


Figure 4. Cartoons of torus and disk+outflow models: (a) smooth models (Fritz et al. 2006), (b) clumpy models (Nenkova et al. 2008a, 2008b; Hönlig & Kishimoto 2010) and, (c) disk + outflow clumpy models (Hönlig & Kishimoto 2017). For smooth models: viewing angle i (degrees) = [0–90], angular width Θ (degrees) = [20–60], parameter of the dust distribution γ = [0–6], and the outer-to-inner radius ratio $Y = R_{\text{out}}/R_{\text{in}} = [10 - 150]$. For clumpy models: viewing angle i (degrees) = [0–90], angular width σ (degrees) = [15–70], number of clouds along the equatorial line $N_0 = [1-15]$ (for Nenkova08) and [2.5–10] (for Hoening10), parameter of radial distribution ($\propto r^{-q}$, in Nenkova08) $q = [0-2.5]$, and parameter of radial distribution ($\propto r^a$, in Hoening10) $a = [-2.5-0]$, the outer-to-inner radius ratio $Y = R_{\text{out}}/R_{\text{in}} = [5-100]$ (for Nenkova08), and $R_{\text{max}} = 170R_{\text{in}}$ (for Hoening10). For disk+outflow clumpy models: viewing angle i (degrees) = [0–90], number of clouds along the equatorial line $N_0 = [2.5-10]$, half-opening angle of the outflow σ_{Θ} (degrees) = [30–45], and angular width of the disk (degrees) $\Theta_w = [7.0-15]$. For a more detailed comparison between the parameters of the models, see González-Martín et al. (2019a, 2019b).

In Figures 5 and 6, we plot the wavelength of the peak of the both 10 and 18 μm silicate features and the strengths of both silicate features as predicted by the models and as observed in the AGN-dominated IRS/*Spitzer* spectra of the Si–s sample. Additionally, we color-coded the objects according to their bolometric luminosity, which we estimate using the hard X-ray luminosity and the relation derived by Marconi et al. (2004) and Alexander & Hickox (2012).

Since the models are probabilistic in nature, we compare the envelope of measurements performed on the models to the measurements of the Si–s AGN sample. While the Fritz 06,

Stalev16, and Nenkova08 models’ envelope covers the wavelength space (Figure 5) where our Si–s AGN measurements lie, the Hoening10 and Hoening17 models miss one and two objects, respectively, with the lowest value central wavelength of the 18 μm silicate feature. Curiously, these objects are of low bolometric luminosity (OQ 208 and NGC 4258).

For the silicate strengths (Figure 6), we note that the range of synthetic values sampled by the models mostly match the observations. However, we also note that the Hoening10 and Hoening17 models show a narrower range of values with respect to the other models. Additionally, the Hoening17 model never predicts both silicates in absorption. Similar results were reported for a larger sample of AGNs (González-Martín et al. 2019b). Finally, all of the models tend to produce extremely prominent silicate emission features that have not been observed.

In Figure 7, we compare the synthetic and observed silicate strength of the 10 μm silicate feature with the α_{NIR} and α_{MIR} spectral indexes. We note that the range of synthetic values sampled by the Fritz06, Hoening10, and Hoening17 models mostly matches the observations, independently of the bolometric luminosity. However, the Nenkova08 and Stalev16 models miss several of the NIR and MIR spectral indexes observed. Note that NGC 3998 is excluded from the plots in Figures 5, 6, and 7 because of the short spectral range ($\sim 7.5-14.5 \mu\text{m}$) covered by the low-resolution IRS/*Spitzer* spectrum of this object.

4.2. Modeling

We apply the torus models using the computational spectral fitting tool XSPEC, which is part of the HEASOFT⁹ software. These models were recently converted into the XSPEC format in order to fit data in a similar way (see Section 2 in González-Martín et al. 2019a). We also use the set of synthetic stellar and empirical H II components (ISM) previously converted into XSPEC format (González-Martín et al. 2019a). The former corresponds to a stellar population of 10^{10} yr and solar metallicity from the stellar spectral libraries of Bruzual & Charlot (2003), while the empirical H II components are average starburst templates from Smith et al. (2007).

We model the AGN-dominated IRS/*Spitzer* spectrum of each object in the Si–s sample, using each one of the four torus family models and the disk+outflow models. Additionally, we add a stellar synthetic and/or H II empirical component to investigate in which cases adding one or both components really improves the fitting. We also add foreground extinction to the torus models by using the ZDUST component (Pei 1992).

In detail, we start converting the IRS/*Spitzer* spectra into the XSPEC format, loading the data into XSPEC, removing the parts of the spectra dominated by emission lines, and modeling the spectra assuming the following component combinations:

1. AGN dust emission: torus models or disk+outflow model
2. AGN + stellar
3. AGN + H II
4. AGN + stellar + H II

For each step, we save the reduced χ^2_{red} , the parameters of the model with their uncertainties, and the emission contribution of each component to the total emission of the IRS/*Spitzer*

⁹ <https://heasarc.gsfc.nasa.gov>

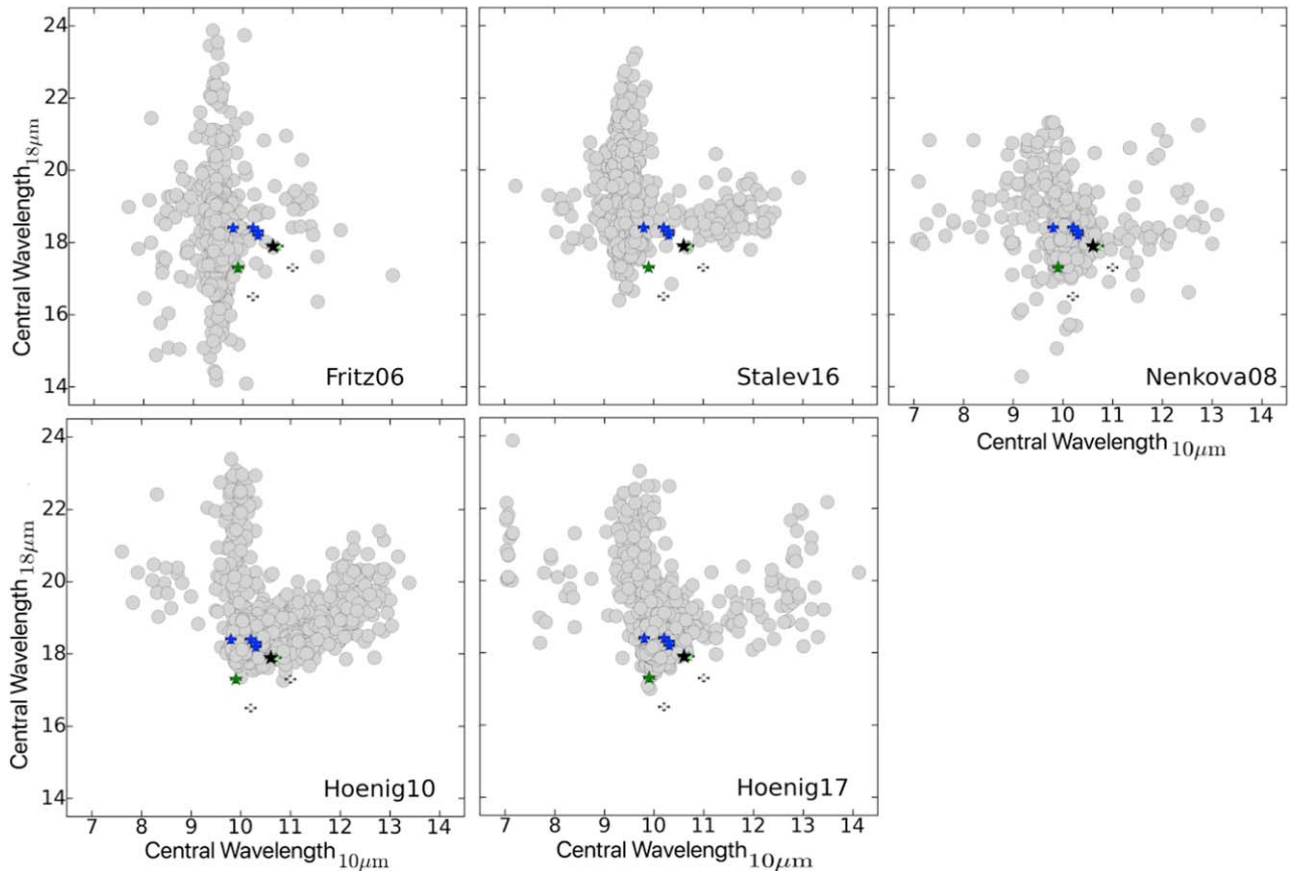


Figure 5. Central wavelength of the synthetic and observed peaks of the 10 and 18 μm silicate features. Gray circles represent the values measured in the models, while the stars are the measurements obtained from the AGN-dominated IRS/*Spitzer* spectra of the Si-s sample. The colors of the stars indicate different range of bolometric luminosities (L_{bol}). White stars are for $\log L_{\text{bol}} < 42$, light-green stars are for $43 \leq \log L_{\text{bol}} < 44$, blue stars for $44 \leq \log L_{\text{bol}} < 45$, green stars for $45 \leq \log L_{\text{bol}} < 46$, and black star for $\log L_{\text{bol}} > 46$. Small stars indicate lower luminosities, while larger stars are for higher luminosities.

spectrum between 5.5 and 30 μm . In those cases where $\chi_{\text{red}}^2 > 2$, we reported the case as “non-modeled.” We perform this procedure for each torus model, resulting in 20 spectral fits per object. Figure 8 shows, for each torus model, the number of spectral fits obtained, using one, two, or three components. Those cases in which none of the component combinations (1–4) are able to model the spectrum with a $\chi_{\text{red}}^2 < 2$ are called “non-modeled” spectral fits (see Appendix C). In the next section, we investigate which model best fits the peak and strength of both silicate emission features in the Si-s sample.

4.3. Model Comparison

In most cases, we find that the same object can be modeled assuming one (AGN), two (AGN+stellar or AGN+H II), or three components (AGN+Stellar+H II) with a $\chi_{\text{red}}^2 \sim 1$. For each object and torus model, we use the statistical f -test, which allows us to evaluate in which cases the addition of a new component improves the fit from a statistical point of view. We add a new component when the f -test probability is $< 10^{-4}$. The computational tool XSPEC includes the FTEST command line, which allows us to calculate the f -statistic and its probability, when new and old values of χ^2 and the degrees of freedom (dof) are provided. As an example, in Figure 9, we show the best fit of the IRS/*Spitzer* spectrum of PG 0844+349 for each torus model. For this particular object, the Fritz06, Nenkova08, and Stalev16 models need an additional stellar component to fit the spectrum, while the Hoenig10 and Hoenig17 models need

also the H II component. Additionally, for this object, we observe that clumpy and disk+outflow models produce the flattest residuals within the uncertainties and smaller χ_{red}^2 (see bottom panel in Figure 9 and Table 3).

In Figure 10, we plot the histogram of the fractional contribution of each spectral component. The AGN component dominates the emission in all cases, which is expected due to our selection of AGN-dominated IRS/*Spitzer* spectrum sources.

Fritz06 models are able to reproduce the IRS/*Spitzer* spectra in seven of ten objects. The AGN component contributes more than 93%. The Nenkova08 models reproduce the IRS/*Spitzer* spectra of ten objects, in most cases with an AGN contribution $> 81\%$, except for NGC 4258, for which the AGN component contributes 66%. For the Hoenig10 models, we find that four of the objects can be modeled with an AGN contribution $> 80\%$, and three other (PG 2214+139, PG 0804+761, and NGC 4258) with a contribution between 67 and 76%. The Hoenig17 models are able to fit seven of the objects with an AGN contribution $> 87\%$, and NGC 4258 with an AGN component that contributes $> 62\%$. Finally, in the case of two-phase medium models of Stalevski et al. (2016) only five of the ten objects can be reproduced with a contribution of the AGN $> 82\%$.

Irrespective of the model used, NGC 4258 always needs a large ($\sim 20\%–38\%$) contribution from the H II component. It is possible that in this case, the spectral decomposition tool DEBLENDIRS is not perfectly separating the different spectral

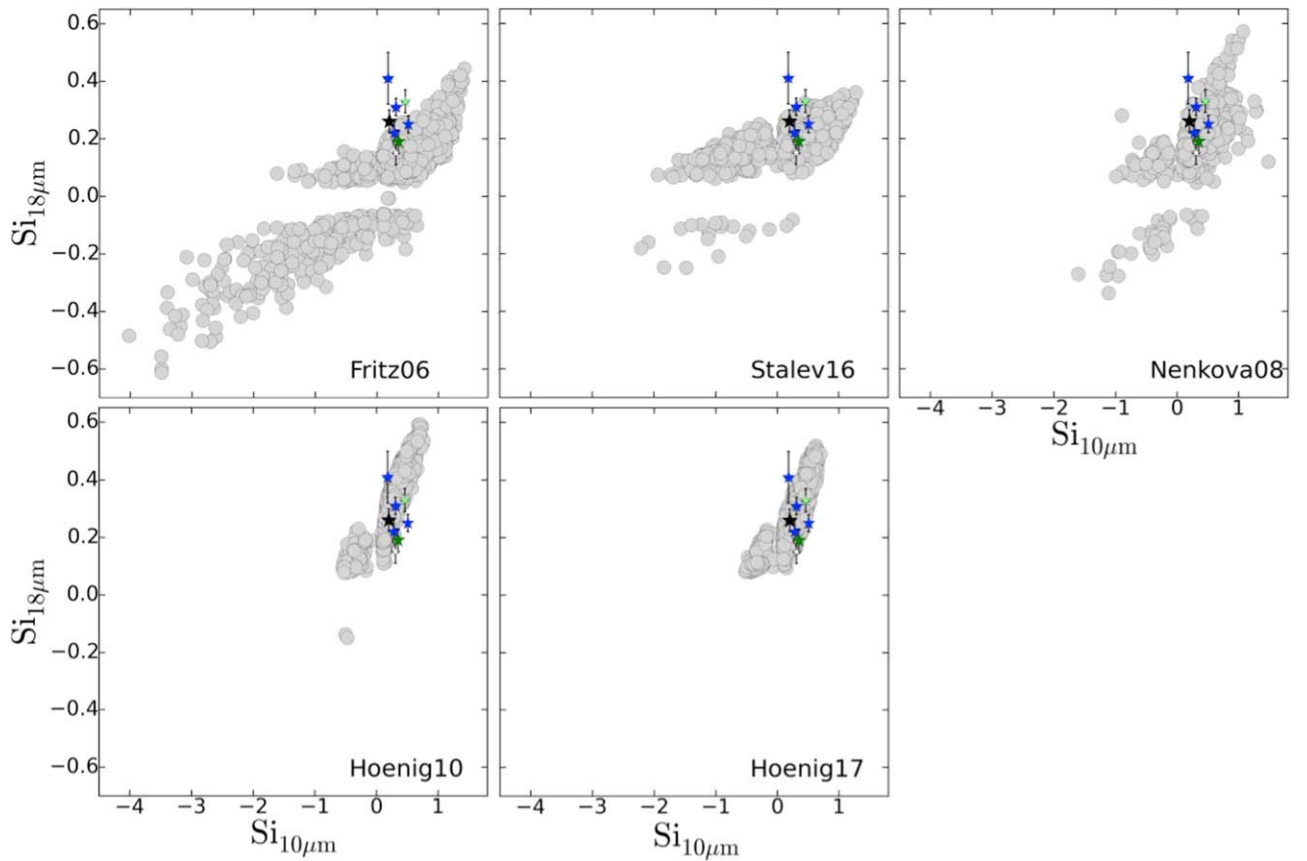


Figure 6. Silicate strength of the 10 and 18 μm silicate features. Symbols and colors are as in Figure 5.

contributions at MIR. We also note that in all cases, the stellar component is necessary to take into account the emission in the bluer extreme of the spectrum, while the H II component is necessary to take into account the emission in the redder extreme of the spectrum. A similar result was also found by González-Martín et al. (2019a) for a large sample of AGNs.

We obtain upper (or lower) limits of the resulting free parameters and covering factors. The covering factor is defined as $1 - P_{\text{esc}}$, where P_{esc} is the probability that a photon emitted in the central engine is able to escape without being absorbed by the torus (in the case of the smooth torus and two-phase medium torus models) or by a dusty cloud in clumpy torus models (Nenkova08, Hoenig10). In the case of the Hoenig17 models, the covering factor derived is the sum of the geometrical covering factors of the disk and the covering factor of the outflow (see González-Martín et al. 2019b).

To obtain well-constrained parameters, a detailed modeling that includes NIR and far-infrared data is necessary (see, e.g., Ramos Almeida et al. 2014). However, simultaneously modeling the NIR and MIR components of the IRS/*Spitzer* spectrum of type 1 AGNs has been a challenge (e.g., Mor et al. 2009; Hernán-Caballero et al. 2015; Martínez-Paredes et al. 2017). In this work, we assume the NIR as a stellar component. Our purpose is to show if any of the proposed models are able to explain both the peak and shape of the strongest silicate emission features. For this purpose, we only need to check that the range of values of the covering factors obtained from modeling the IRS/*Spitzer* spectra with each model is within the range of values expected for type 1 AGNs (see, e.g., Alonso-Herrero et al. 2011; Ramos Almeida et al. 2011; Ichikawa et al. 2015; Mateos et al. 2016; González-Martín et al. 2017; Martínez-Paredes et al. 2017).

We note that on average, the smooth models produce a dusty torus with small angular widths, with low and high viewing angles; although, the angular width is poorly constrained. The dusty clumpy torus models of Nenkova08 produce both large and low viewing angles and a range of angular widths from low (15°) to high (70°) values, and a number of clouds along the equatorial ray that are in general $\lesssim 7$ clouds, resulting in escape probabilities $\gtrsim 40\%$. The clumpy models of Hoenig10 produce values of the viewing angle that range from nearly 30° to 80° , angular widths around 55° , and number of clouds in the range 2.5–10.0. The viewing angles in disk+outflow models of Hoenig17 that we find are between 0° and 50° , and the angular widths are between 30° and 45° . Although in three cases, we obtain lower limits of the angular width, indicating that this could be larger. The two-phase models of Stalev16 produce on average large viewing angles ($\sim 80^\circ$), only in one case we obtain a viewing angle around 10° , and the angular width is around 80° , resulting in very obscured AGNs (see Tables 6–10, and Figure 17 in Appendix C).

In general, Fritz06 and Hoenig17 models produce lower covering factors than the Nenkova08, Hoenig10, and Stalevski16 models. The Fritz06 and Hoenig17 models produce covering factors around 0.2, although they range from 0 to 1. The Nenkova08 model produces covering factors around 0.6 with a range from 0.3 to 1.0. These values are consistent with the range of values obtained by Martínez-Paredes et al. (2017) for a sample of PG QSOs using Nenkova08 models. Feltre et al. (2012) compare smooth and clumpy torus models of Nenkova08 and found that both torus model families produce similar MIR continuum shapes for different model parameters. In the Hoenig10 and Stalevski16 models, the covering factors

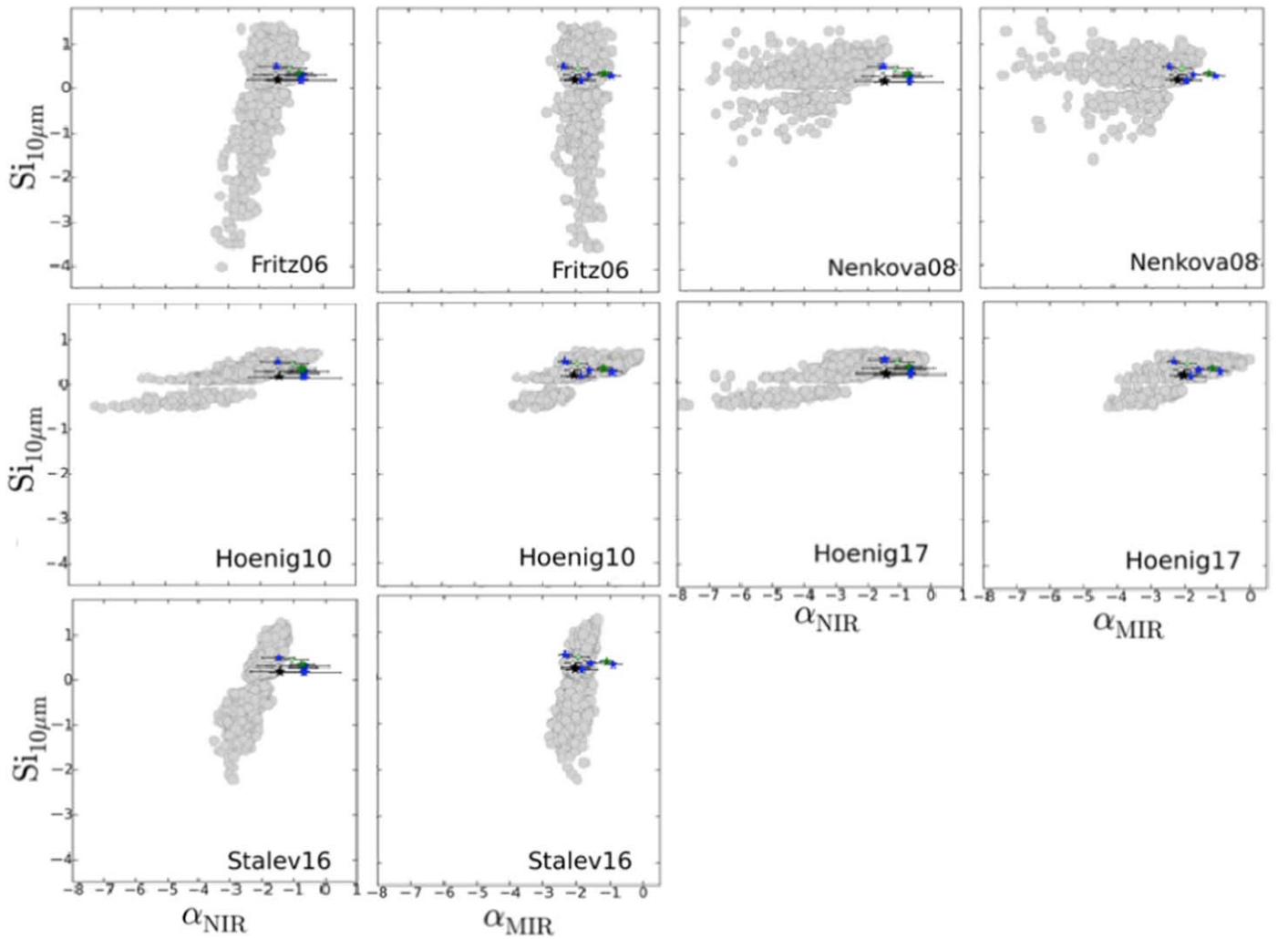


Figure 7. Synthetic and observed silicate strength of the $10\ \mu\text{m}$ silicate feature, and the NIR α_{NIR} and MIR α_{MIR} , spectral indexes. Symbols and colors are as in Figure 5.

are large (around 0.8), probably due to the fact that, in these models, the angular width of the torus tends to be larger, which leads to a more obscured AGN.

4.4. Residuals

Using the spectral residuals for all modeled and non-modeled cases, we calculate the average spectral residuals for each torus model. The vertical black solid lines in Figure 11 represents the mean wavelength where the silicate features peak in the IRS/*Spitzer* spectra, and the black dotted lines their 1σ intervals.

In order to discuss qualitatively the similarities and differences between the residuals of the models, we divide the spectral range into three parts in Figure 11. These parts are the region bluewards of $10\ \mu\text{m}$, between 10 and $18\ \mu\text{m}$, and redwards $18\ \mu\text{m}$. In part (a), we observe that on average, around $5\ \mu\text{m}$, the Fritz06, Nenkova08, Hoenig10, and Stalev16 models are the worst at reproducing the bluer extreme of the spectra within the uncertainties. However, at longer wavelengths, the Fritz06 and Stalevski16 models are the least accurate at reproducing the shape of the spectra. The Hoenig17 models best reproduce the spectra at all wavelengths within the uncertainties. In part (b), Nenkova08 show the flattest residual,

while in the redder extreme, the Fritz06 and Stalevski16 models show the largest residuals, while the Hoenig10 and Hoenig17 models shows flatter residuals. In part (c), all models show similar residuals, although Nenkova08 shows the flattest residual within the uncertainties.

We also observe that the Fritz06 and Stalevski16 models underestimate the strength of the 10 and $18\ \mu\text{m}$ silicate features, while the Nenkova08, Hoenig10, and Hoenig17 models best reproduce the peak and the shape of both features. In general, we note that the Hoenig17 and Nenkova08 models show flatter residuals, resulting in the models that best reproduce the shape and peak of the strong silicate features observed in these objects.

Some objects deserve particular attention. For instance, in Figure 19, we can see that for NGC 7213, we require the stellar component to fit the bluer extreme of the spectrum but that both silicate peaks are still underestimated by the Nenkova08 models.

PG 1351+640 is modeled only by the smooth and clumpy models of Nenkova08. In both cases it is necessary to add the stellar component, which contributes 3% and 1% in the case of smooth (Fritz06) and clumpy models (Nenkova08 and Hoenig10), respectively. OQ208 is modeled only by the

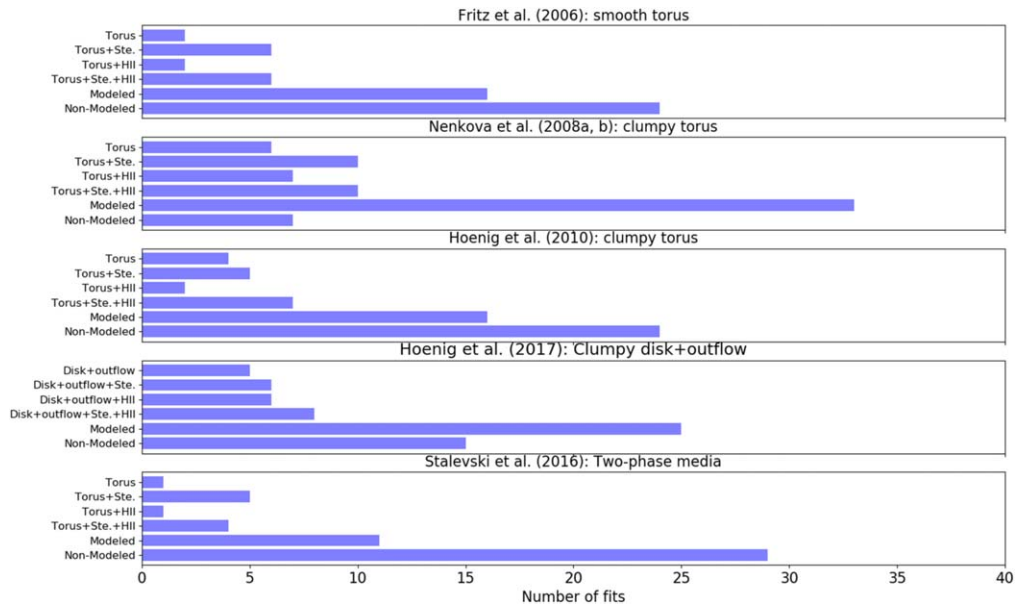


Figure 8. Fitting components for each torus model: from top to bottom, the horizontal bars show the number of fits with one (AGN), two (AGN + stellar or AGN + H II), and/or three (AGN + stellar + H II) components for each dusty torus model. Additionally, for each torus model, the two last horizontal bars represent the total number of cases modeled and not modeled ($\chi_{\text{red}}^2 > 2$), respectively.

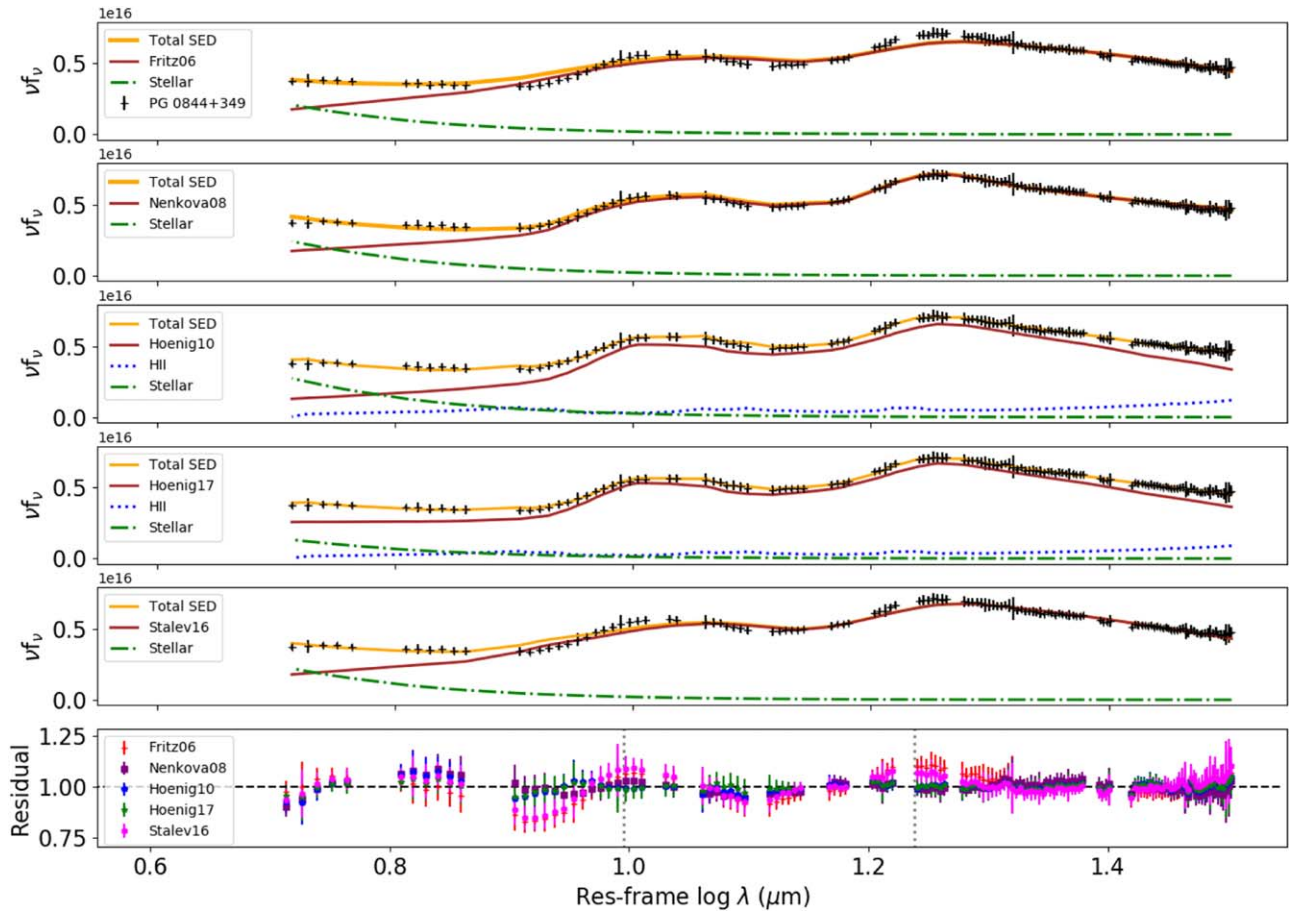


Figure 9. Modeling and residuals of the IRS/Spitzer spectrum of PG 0844+349. From top to bottom, we assume models Fritz06 ($\chi_{\text{red}}^2 \sim 1.20$), Nenkova08 ($\chi_{\text{red}}^2 \sim 0.32$), Hoenig10 ($\chi_{\text{red}}^2 \sim 0.20$), Hoenig17 ($\chi_{\text{red}}^2 \sim 0.13$), and Stalevski16 ($\chi_{\text{red}}^2 \sim 0.81$). The χ_{red}^2 values refer to fits with both torus models and other components. The last panel shows the residuals defined as the ratio between the data and model. In all panels, the black points are the IRS/Spitzer spectrum and its error in $\text{erg s}^{-1} \text{cm}^{-2}$, and the red solid line is the fitted torus model. The orange line is the total SED that results when the stellar (green dotted–dashed line) and/or the H II (blue dotted line) components are added to model the spectrum.

Table 3
Best Fits from Smooth Models

Name	χ^2_{red}	Best Combination	Component Contributions			Name	χ^2_{red}	Best Combination	Component Contributions		
			AGN (%)	Stellar (%)	H II (%)				AGN (%)	Stellar (%)	H II (%)
Smooth torus models of Fritz et al. (2006)						Disk+outflow models of Hönic & Kishimoto (2017)					
PG 2304+042	1.92	Torus+Stellar	93	7	0	PG 2304+042	0.57	Disk+outflow+Stellar	93	7	0
PG 0844+349	1.20	Torus+Stellar	93	7	0	PKS 0518-45	0.31	Disk+outflow	100	0	0
PG 1351+640	1.52	Torus+Stellar	97	3	0	PG 0844+349	0.13	Disk+outflow+Stellar+H II	87	5	8
PG 2214+139	1.52	Torus+Stellar	96	4	0	PG 2214+139	0.20	Disk+outflow+Stellar+H II	95	1	4
PG 0804+761	0.63	Torus+Stellar	94	6	0	PG 0804+761	0.49	Disk+outflow+H II	95	0	5
NGC 3998	1.91	Torus+Stellar	100	0	0	OQ 208	1.78	Disk+outflow+Stellar	98	2	0
.	NGC 4258	1.88	Disk+outflow+H II	62	0	38
.	NGC 3998	0.39	Disk+outflow	100	0	0
Clumpy torus models of Nenkova et al. (2008a, 2008b)						Two-phase media torus models of Stalevski et al. (2016)					
NGC 7213	1.11	Torus+Stellar	96	4	0	PG 2304+042	1.99	Torus+Stellar	93	7	0
PG 2304+042	1.25	Torus+Stellar	92	8	0	PKS 0518-45	1.65	Torus	100	0	0
PKS 0518-45	1.29	Torus+Stellar	97	3	0	PG 0844+349	0.81	Torus+Stellar	92	8	0
PG 0844+349	0.32	Torus+Stellar	91	9	0	PG 2214+139	0.91	Torus+Stellar+H II	82	10	8
PG 1351+640	1.92	Torus+Stellar	99	1	0	PG 0804+761	1.11	Torus+Stellar	90	10	0
PG 2214+139	1.92	Torus+Stellar	87	13	0
PG 0804+761	1.60	Torus+Stellar	89	11	0
OQ 208	0.32	Torus+Stellar+H II	91	3	6
NGC 4258	0.78	Torus+Stellar+H II	66	4	30
NGC 3998	0.32	Torus+Stellar	81	19	0
Clumpy torus models of Hönic & Kishimoto (2010)					
PG 2304+042	1.18	Torus	100	0	0
PKS 0518-45	0.46	Torus+Stellar+H II	89	6	5
PG 0844+349	0.20	Torus+Stellar+H II	80	10	10
PG 2214+139	0.71	Torus+Stellar+H II	76	9	14
PG 0804+761	1.79	Torus+Stellar+H II	76	9	15
NGC 4258	1.64	Torus+Stellar+H II	67	3	29
NGC 3998	0.40	Torus	100	0	0

Note. Column 1 lists the name of the object, column 2 the χ^2_{red} , column 3 the combination of components that best fit the IRS/*Spitzer* spectra, and columns 4–6 the percentage contribution of each component.

Nenkova08 and Hoenic17 models. In this case, the residuals from the Nenkova08 model are flatter than the residuals from the Hoenic17 models, although in the case of the Nenkova08 model, it is necessary to include the H II component with a contribution of 6%, in addition to the stellar component (3%) in order to fit the redder extreme of the spectrum. In contrast, the Hoenic17 model is able to reproduce the entire spectral range requiring only a small contribution from the stellar component (2%). The remaining objects are modeled successfully by the Nenkova08, Hoenic10, and Hoenic17 models.

We divide the objects in the Si-s sample into three groups according to their bolometric luminosities and BH accretion rates. For each group and torus model, we combine the residual obtained from fitting the AGN-dominated *Spitzer* spectrum with the components C1 (AGN), C2 (AGN+Stellar), C3 (AGN+H II), and C4 (AGN+Stellar+H II). In Figure 12, we plot the average residual for each group. We note that for the first group, all models are unable to produce a flat residual around the 10 μm silicate feature. But, for the second group, which covers a larger range of bolometric luminosities and BH accretion rates, all of the residuals become flatter. At the largest bolometric luminosities of the third group, all models show the flattest residuals. These results show that all models fail in

reproducing the central wavelength of the 10 μm silicate feature in the objects with lower bolometric luminosities, as we see in Figure 5 in Section 4.1. Additionally, we note that the Hoenic17 models always produce the flattest residual around 5 μm for low, intermediate, and high luminosities.

5. Discussion

In the previous section, we used four different torus models (smooth, clumpy, two-phase medium, and disk+outflow) to reproduce the strongest silicate features observed in type 1 AGNs. These features appear broader and shifted with respect to the silicate emission features observed in the standard ISM, suggesting a different dust composition (or geometry) of the torus or surrounding dust of AGNs. We discuss below the dust distribution (Section 5.1) and composition (Section 5.2) of the dust. We also discuss the deficiencies of the models to reproduce the strong silicate emission features in Section 5.3.

5.1. Dust Distribution

Based on our analysis, the clumpy models of Nenkova08 ($\chi^2_{\text{red}} \sim 1.03$), Hoenic10 ($\chi^2_{\text{red}} \sim 0.89$), and Hoenic17 ($\chi^2_{\text{red}} \sim 0.70$) produce a better fitting of the IRS/*Spitzer*

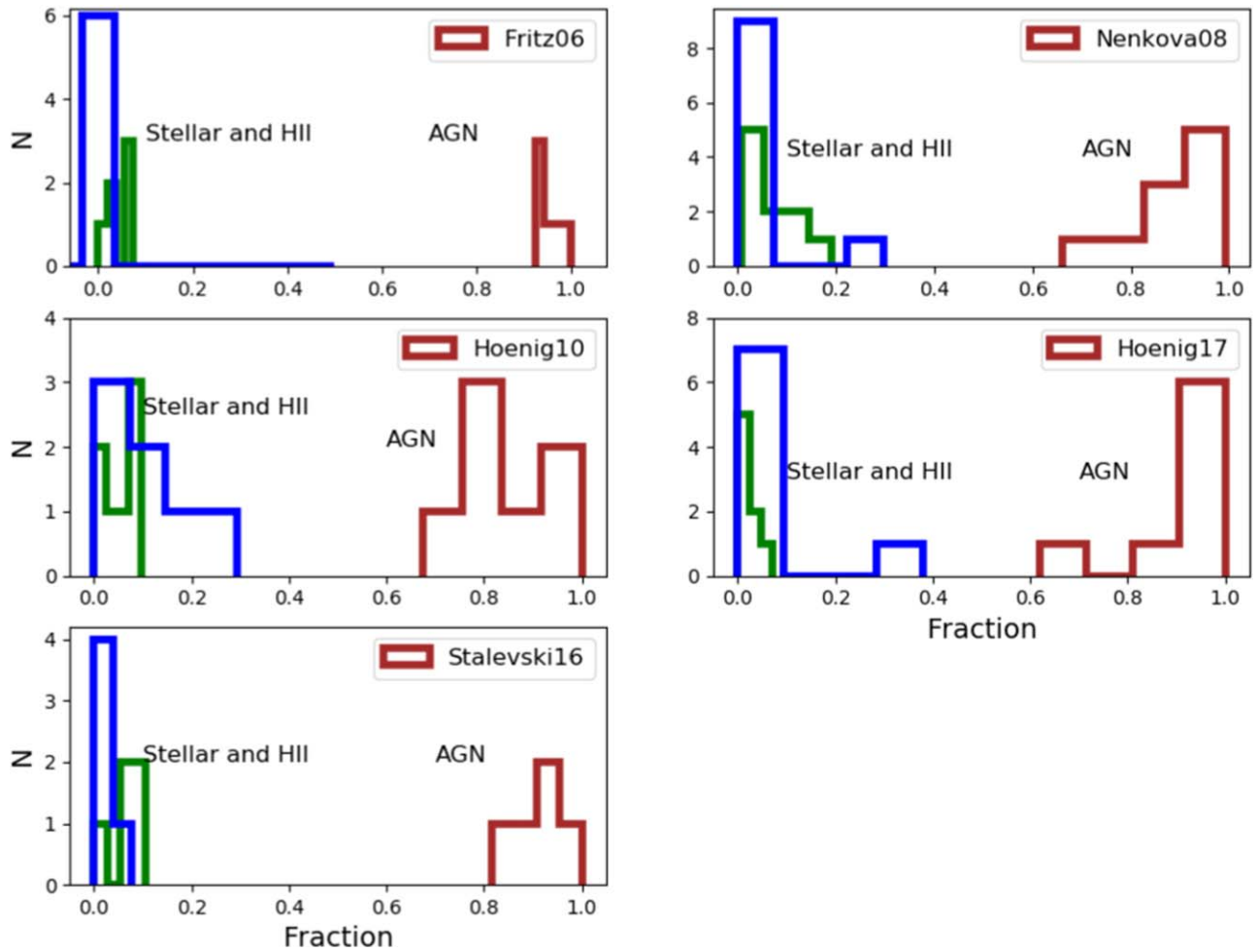


Figure 10. Fractional contributions of the AGN (brown histogram), stellar (green histogram), and H II (blue histogram) components for [Fritz06](#), [Nenkova08](#), [Hoenig10](#), [Hoenig17](#), and [Stalevski16](#) models.

spectra than the smooth ($\chi_{\text{red}}^2 \sim 1.36$) and two-phase medium ($\chi_{\text{red}}^2 \sim 1.20$) models. This result is in agreement with the previous evidence that the surrounding medium around the AGN should be clumpy (see [Ramos Almeida & Ricci 2017](#), and references therein). Indeed, [Mendoza-Castrejón et al. \(2015\)](#) found that isolated type 1 AGNs have a clumpy dust distribution, while interacting type 1 AGNs can have both clumpy or smooth dusty distributions. Additionally, we find that all models produce flatter residuals in high-luminosity AGNs than in low-luminosity AGNs, probably due to all models better sampling the central wavelength and both 10 and 18 μm silicate features of high-luminosity AGNs. However, high-luminosity [Hoenig17](#) models produce the flattest residuals along the entire spectral range.

[Mor et al. \(2009\)](#) used IRS/*Spitzer* spectra of a sample of 26 nearby QSOs to constrain the clumpy models of [Nenkova08](#). They argue that in order to model the entire spectral range between 5 and 30 μm , they need to add two more components, one that takes into account the emission produced by the dust in the narrow-line region ([Schweitzer et al. 2008](#)), and another one that takes into account the emission produced by dust close to the AGN, not directly related with the dusty torus (e.g., [Minezaki et al. 2004](#); [Kishimoto et al. 2007](#); [Riffel et al. 2009](#)). However, [Alonso-Herrero et al. \(2011\)](#) showed, for a sample of local Seyferts, that when high angular resolution data at NIR

and MIR is used, it is not necessary to add any additional components in order to constrain the clumpy models of [Nenkova08](#); although, for some type 1 Seyferts galaxies, they found that the NIR emission is underpredicted by the fitted SED. In a previous work, we used the starburst-subtracted IRS/*Spitzer* spectra from ~ 7.5 to 15 μm plus NIR high angular resolution data from the Near Infrared Camera and Multi-Object Spectrometer on *Hubble Space Telescope* for a sample of 20 nearby QSOs in order to constrain the clumpy torus models of [Nenkova08](#). [Martínez-Paredes et al. \(2017\)](#) found that including the spectral range between 5 and 8 μm resulted in a poor fitting of the 10 μm silicate emission feature. In this work, we find that the AGN-dominated *Spitzer* spectra of the Si-s type 1 AGN can be fitted by [Nenkova08](#) and/or [Hoenig10](#) models by adding a stellar component that takes into account the bluer spectral range, and in some cases, the H II component, in order to improve the fitting in the redder spectral range. A similar result was also found for a large sample of AGNs ([González-Martín et al. 2019a, 2019b](#)).

[Hernán-Caballero et al. \(2017\)](#) found, for a sample of 85 QSOs, that a superposition of two blackbodies between 1.7 and 8.4 μm , with temperatures around 1000 K for the hot blackbody component, and 400 K for the warm blackbody component, can fit the *Spitzer* spectra between 0.1 and 10 μm . They argue that an additional hotter component of dust is necessary to reproduce the excess emission at 1–2 μm . On the

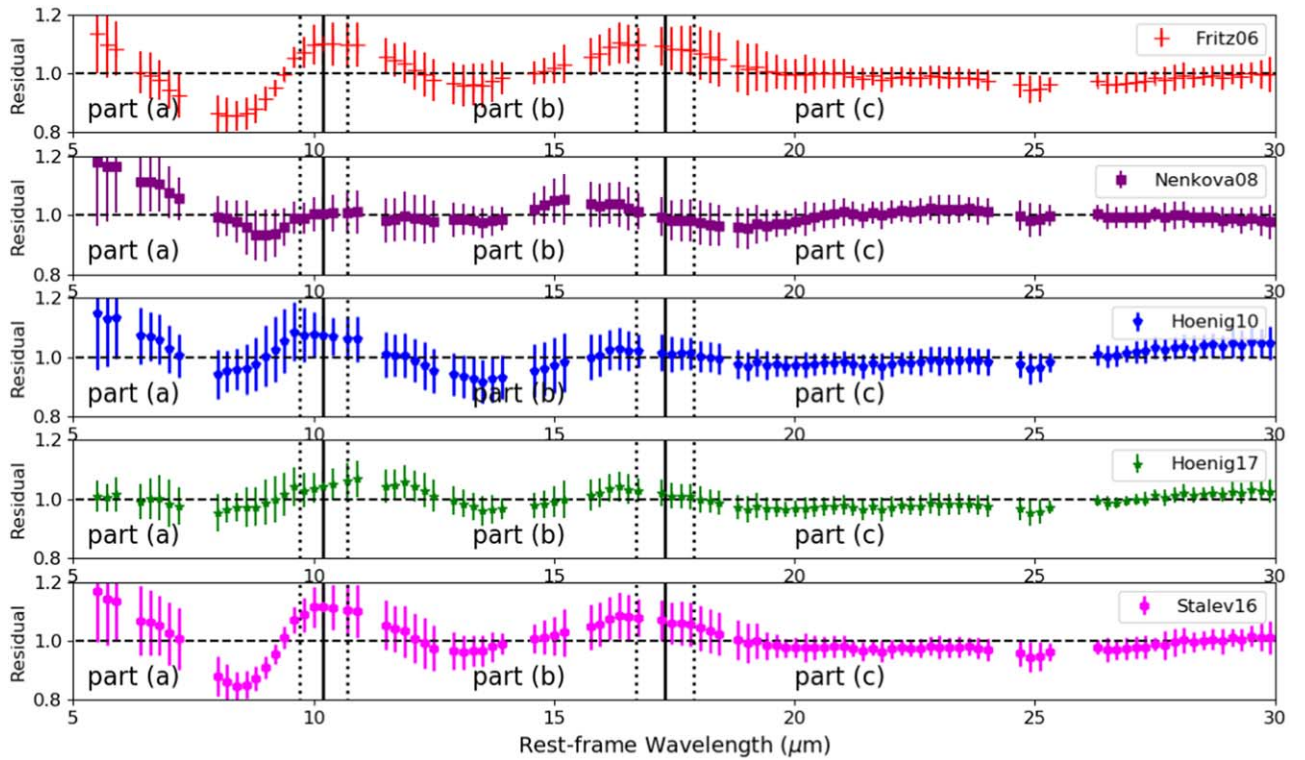


Figure 11. Average residuals (data/model) for all modeling combinations, including the modeled and non-modeled cases. The red points represent the average residuals of objects fitted with the smooth models. The purple and blue points represent the average residuals obtained from those objects fitted with the clumpy models of Nenkova08 and Hoenig10, respectively. The green points represent the average residuals obtained from the objects fitted using the disk+outflow (Hoenig17) models, and the magenta points are the residuals obtained from using the two-phase dusty torus model of Stalevski16. The vertical gray solid line indicates the mean wavelength where the 10 and 18 μm silicate features peak. The gray dashed lines are the 1σ confidence intervals.

other hand, Lyu et al. (2017) argues that the strong silicate emission features observed in dust-deficient PG QSOs can be explained assuming a reduced height scale of the warm dust, i.e., the dust between the sublimation zone and the outer region of cold dust, allowing for less interception of the radiation from the accretion disk with the inner dust, resulting in a decrease of the MIR continuum, but keeping the heating of the outer dust responsible for the silicate emission features invariant (see Figure 20 in Lyu et al. 2017).

5.2. Dust Composition

In general, the Nenkova08 models produce a better fit than the Hoenig10 ones. They assume the same geometry, but the former uses a standard dust composition, while the latter includes standard ISM dust plus standard ISM with large grains and also a composition of dust mostly dominated by graphite. The Hoenig10 models assume this dust composition in order to take into account the observational suggestion that the dust composition in AGNs deviates from standard ISM dust (Suganuma et al. 2006; Kishimoto et al. 2007). One of the clear improvements in the Hoenig17 models is that they allow for the existence of different dust compositions in different parts of the surrounding dusty structure (disk+outflow).

The chemical composition of the dust has been largely studied for the ISM (see Henning 2010, and references therein), and to a lesser extent in AGNs (see Lyu et al. 2014, and references therein). However, determining the exact chemical

composition of the dust has been challenging. Srinivasan et al. (2017) studied the dust composition of a large sample of PG QSOs with a redshift $z < 0.5$, which showed the 10 μm silicate feature in emission. They found that the dust is mostly composed of amorphous oxides and silicates, plus a small fraction in crystalline form. However, this small fraction is nearly four times larger than the last upper limit ($\lesssim 2.2$) reported by Kemper et al. (2005) for the ISM, and more similar to the upper limit ($\lesssim 5$) previously reported by Li & Draine (2001) for the ISM.

5.3. Deficiencies of the Models

In general, we find that neither the peak nor the shape of the silicate features of the AGN-dominated IRS/*Spitzer* spectra of the Si-s type 1 AGN are perfectly reproduced by the models. However, we note that for each object, either the Hoenig17 or the Nenkova08 model produces the smallest χ^2_{red} and flattest residuals. Hönig & Kishimoto (2017) point out that their dust composition explains both the observed small NIR reverberation mapping and interferometric sizes with dust sublimation physics. They argue that this combination of disk+outflow clumpy models is able to reproduce the 3–5 μm bump in type 1 AGNs, and preserve the MIR bump produced by the wind. Indeed, according to this model, a standard ISM composition of the dust in the wind would be responsible for the emission of the silicate features. García-González et al. (2017) found that the Hoenig17 (disk+outflow) models predict MIR slopes

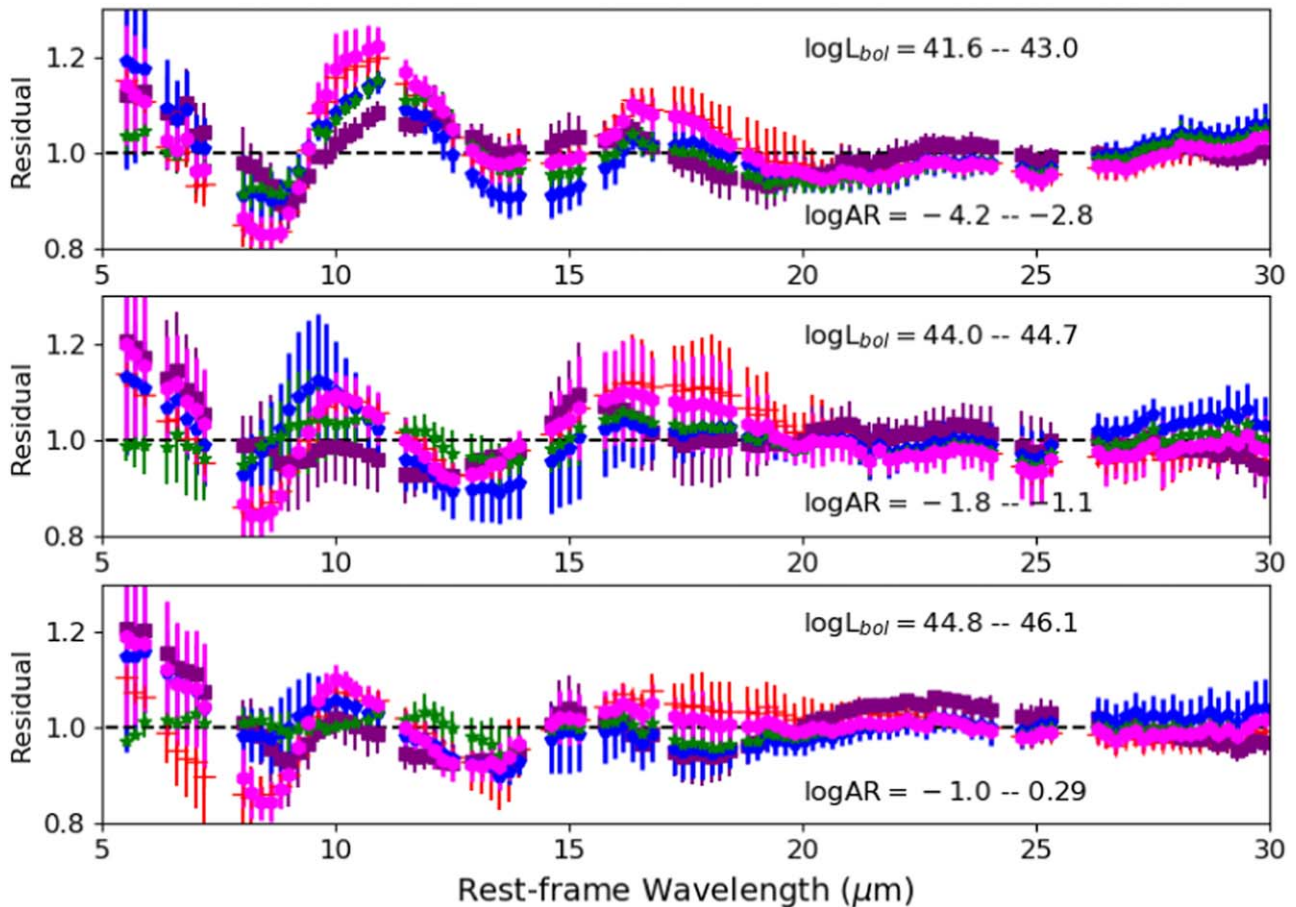


Figure 12. Average residuals for three ranges of bolometric luminosities and BH accretion rates. Colors are as in Figure 11.

(between 8.1 and 12.5 μm) and silicate strengths at 10 μm that are in agreement with the values observed in type 1 AGNs. Particularly, they noted that when clouds are more concentrated toward the inner region of the torus (see, e.g., Hönic & Kishimoto 2010; Ramos Almeida et al. 2011; Ichikawa et al. 2015; Martínez-Paredes et al. 2017), the MIR spectral indices are flatter, and the silicate features are stronger than those observed in Seyferts and QSOs.

6. Summary and Conclusions

In order to investigate which model better reproduces the shape and peak of the strongest 10 μm silicate emission features observed in type 1 AGNs, we measure the 10 μm silicate emission strength for a sample of local ($z < 0.1$) type 1 AGNs, for which their IRS/*Spitzer* spectra is mostly dominated by the emission of nonstellar processes (>80%).

We find that these objects show silicate features in emission. On average, the 10 μm silicate feature has a strength of $0.13^{+0.15}_{-0.36}$ that peaks at 10.3 μm , and an 18 μm silicate strength of $0.14^{+0.06}_{-0.06}$ that peaks at 17.3 μm . We find that 10 objects are among the AGNs with the largest 10 μm silicate strengths ($\sigma_{\text{Si}_{10\mu\text{m}}} > 0.28$, Si-s sample) and that some of them have been previously classified as objects with prominent silicate features.

We use four different torus models, Fritz06 (Fritz et al. 2006), Nenkova08 (Nenkova et al. 2008a, 2008b), Hoenic10

(Hönic & Kishimoto 2010), and Stalevski16 (Stalevski et al. 2016) and a disk+outflow (Hoenig17, Hönic & Kishimoto 2017) model to fit the IRS/*Spitzer* spectra of the Si-s sample and investigate which model better reproduces the peak and shape of both silicate emission features. The models assume different dust distributions, namely, smooth, clumpy, and a two-phase medium, as well as different dust compositions. We find that in most cases, it is necessary to add a stellar or H II component in order to improve the fit. In most cases, we find that the contribution of these components is $\ll 20\%$, in agreement with our selection requirement that the spectra be dominated by the emission of the AGN. The exception is NGC 4258 for which the spectral decomposition seems to underestimate the H II component.

We find that, in general, the Fritz06 and Hoenig17 models produce lower covering factors than the Nenkova08, Hoenic10, and Stalevski17 models. The values are consistent with those reported in previous works for type 1 AGNs. We find that the individual and average spectra are reproduced better with clumpy torus models than smooth models. Moreover, the Hoenig17 model shows the flattest residuals along all of the spectral range between ~ 5 and 35 μm , while the rest of the models fail to reproduce the bluer extreme of the spectrum. However, on average, none of the models are able to exactly reproduce the peak and shape of the silicate features.

In the near future, the Mid-Infrared Instrument (MIRI) on board the *James Webb Space Telescope* will provide high angular resolution with higher sensitivity and spectral resolution observations that will allow for an in-depth investigation of the dust properties in active galaxies. Additionally, new models that include a better description of the properties of the dust will be required.

M.M.-P. acknowledges support by the KASI and UNAM-DGAPA postdoctoral fellowships. This work is partially supported by the KASI project 2019184100 and Conacyt project CB-2016-281948. O.G.-M. acknowledges support by the PAPIIT projects IA100516. A.A.-H. acknowledges support through grant PG C2018-094671-B-I00 (MCIU/AEI/FEDER, UE). Work by A.A.H. was done under project No. MDM-2017-0737 Unidad de Excelencia “María de Maeztu”- Centro de Astrobiología (INTA-CSIC). Y.K. acknowledges support from grant DGAPA-PAPIIT 106518, and from program DGAPA-PASPA. T.H. acknowledges the support from the National Research Foundation of Korea (NRF) grant funded by the Korea government (MSIT; 2019R1A2C1087045). C.R.A. acknowledges financial support from the Spanish Ministry of Science and Innovation (MICINN) through project PN AYA2013-47742-C4-2-P. C.R.A. also acknowledges the Ramon y Cajal Program of the Spanish Ministry of Economy and Competitiveness. This work is based on observations obtained with the *Spitzer Space Observatory*, which is operated by JPL, Caltech, under NASA contract 1407. This research has made use of the NASA/IPAC Extragalactic Database (NED), which is operated by JPL, Caltech, under contract with the National Aeronautics and Space Administration. CASSIS is a

product of the Infrared Science Center at Cornell University, supported by NASA and JPL.

Appendix A Spectral Decomposition

In order to select those type 1 AGNs in which the IRS/*Spitzer* spectrum is mostly (>80%) dominated by emission from dust heated by the AGN, we use the spectral decomposition tool DEBLENDIRS from Hernán-Caballero et al. (2015).

DEBLENDIRS is a spectral decomposition tool that uses a set of starburst, stellar, and AGN templates with IRS/*Spitzer* spectrum. This spectral decomposition assumes that the spectral shape of the AGN and its host galaxy are found in other sources where the emission from the AGN or host galaxy completely dominate the spectral emission. The spectral emission of the host galaxy comprises the stellar emission (passive stellar population) and the emission from the interstellar medium (ISM), e.g., PAH, since the emission of these molecules is related to the presence of young star-forming regions, e.g., starbursts (SB). The spectral decomposition carries on, trying every possible combination between stellar, PAH, and AGN, according to the following linear spectral combination:

$$f_{i,j,k}(\lambda) = af_i^{\text{stellar}}(\lambda) + bf_i^{\text{PAH}} + cf_k^{\text{AGN}}(\lambda), \quad (2)$$

where the i, j , and k indices range all of the stellar, PAH, and AGN templates, respectively. The a , b , and c coefficients are obtained through the χ^2 minimization. In Figure 13, we show an example of the spectral decomposition. After we find the combination of components that best reproduce the IRS/*Spitzer*

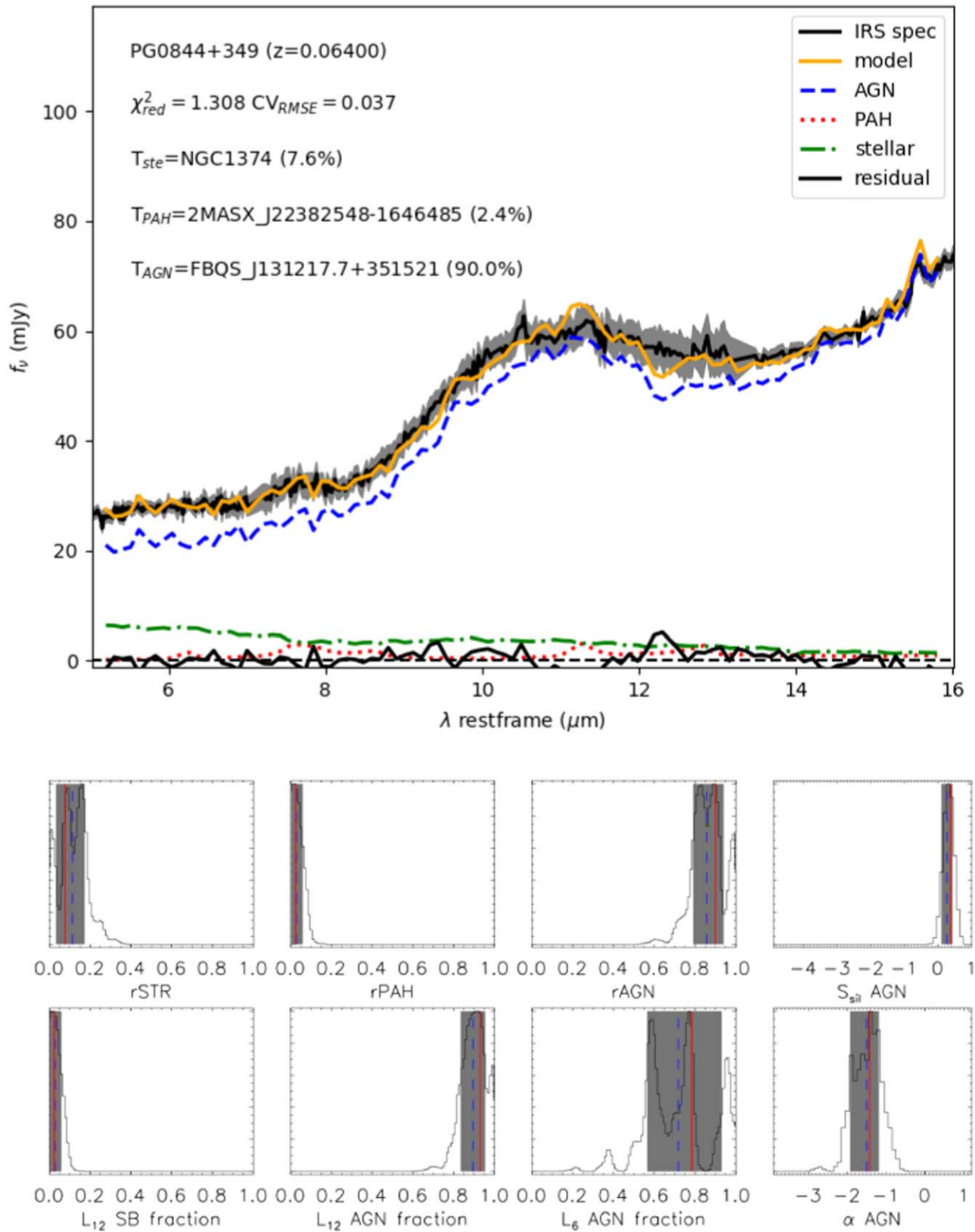


Figure 13. Upper panel: spectral decomposition. The green dotted–dashed, blue dashed, and red dotted lines represent the stellar, starburst, and AGN components, respectively. The orange solid line is the sum of the three components (stellar, starburst, and AGN). The black solid line is the resampled IRS/*Spitzer* spectrum with their errors (gray shadow). The horizontal solid black line around zero is the residual. Bottom panel: probability distributions. r_{STR} , r_{PAH} , and r_{AGN} are the fractional contribution of the stellar, PAH, and AGN components, respectively. L_{12} SB fraction, L_{12} AGN fraction, and L_6 AGN fraction are the monochromatic luminosity of the SB and AGN at 12 and 6 μm , respectively. S_{sil} and α AGN are the silicate strength and the spectral index of the AGN component.

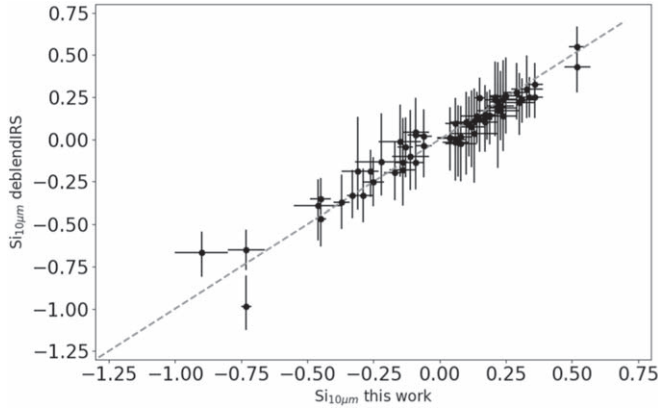


Figure 14. $10\ \mu\text{m}$ silicate strength as measured using our own methodology (see Section 2.3) and deblendIRS. The gray dashed line represents the 1:1 comparison.

spectrum, DEBLENDIRS estimates the fractional contribution of each component to the integrated $5\text{--}15\ \mu\text{m}$ luminosity, the luminosity of the starburst at $12\ \mu\text{m}$, and the luminosity of the AGN at 12 and $6\ \mu\text{m}$. Additionally, it gives, for the AGN component, the silicate strength measured at the wavelength where the silicate feature peaks, and the MIR spectral index measured between 8.1 and $12.5\ \mu\text{m}$. In Figure 14, we compare the $10\ \mu\text{m}$ silicate strength derived from the spectral decomposition with our measurements (see Section 2.3).

Appendix B Silicate Strength Measurements

Here, we report the silicate feature strengths measurements for the full sample. See Table 4 and Figures 15 and 16.

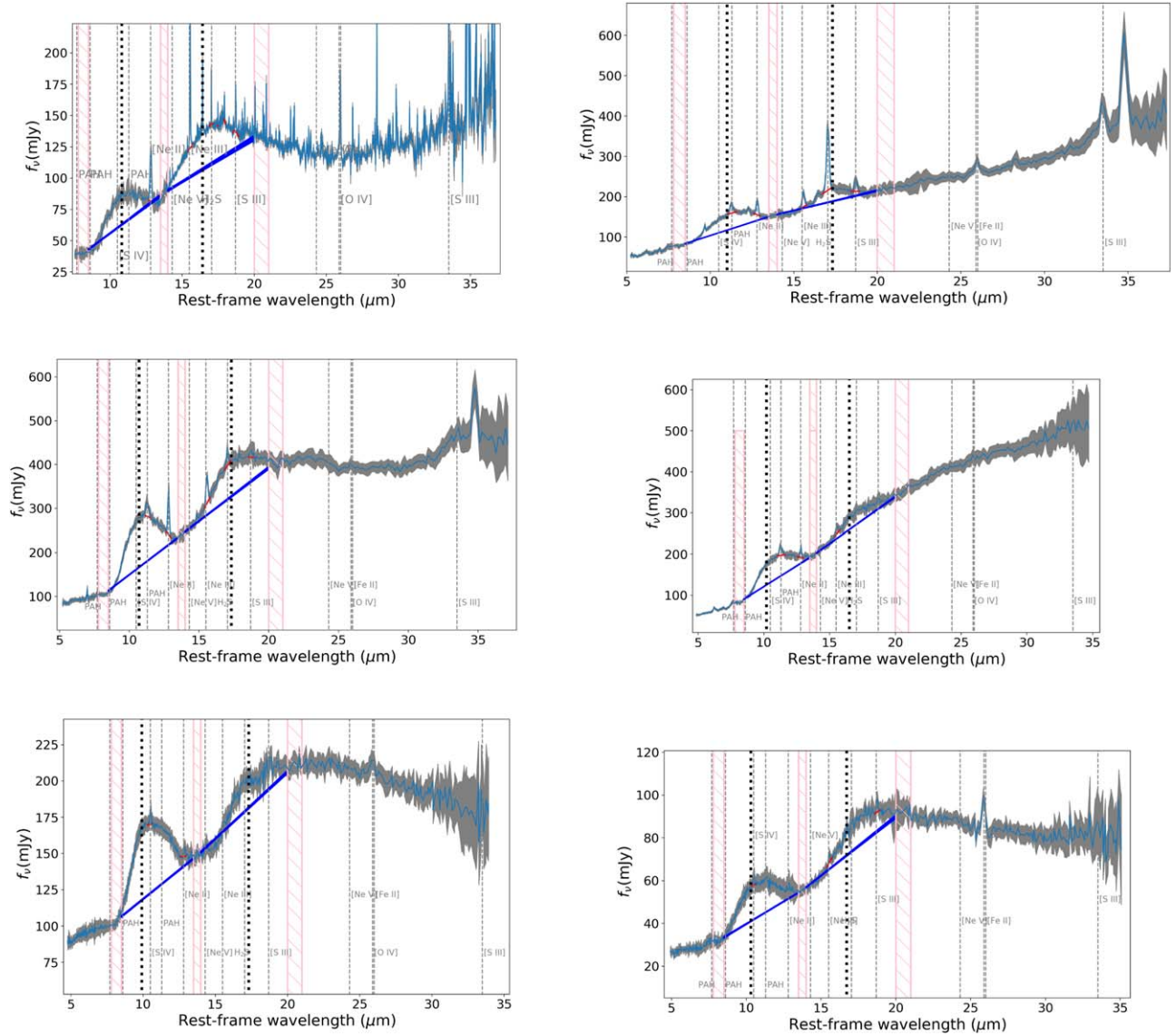


Figure 15. IRS/*Spitzer* spectrum (light blue solid line). Upper panels: NGC 3998 (left panel), NGC 4258 (right panel). Middle panels: NGC 7213 (left panel), OQ 208 (right panel). Bottom panels: PG 0804+761 (left panel), PG 0844+349 (right panel). The red line is the local continuum that follows the broad features of the IRS/*Spitzer* spectrum. The blue solid lines are the bootstrapped local continua, and the vertical pink dashed bars are the bands used to fit the continua around the features. The vertical black dashed lines indicate the wavelength where the silicate strength is measured. The vertical gray dashed lines mark other emission lines. For NGC 3998, the spectrum between 14 and $35\ \mu\text{m}$ is the high angular resolution spectrum from *Spitzer*.

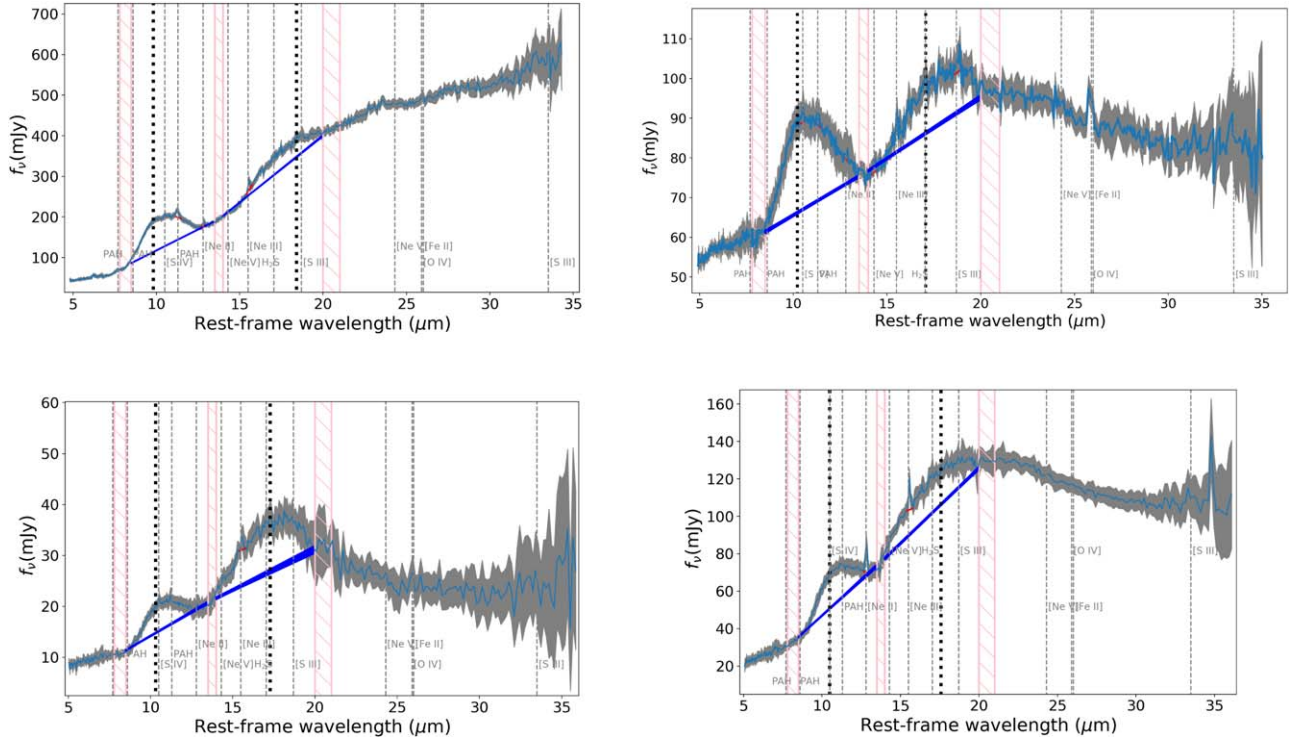


Figure 16. IRS/*Spitzer* spectrum. Upper panels: PG 1351+640 (left panel), PG 2214+139 (right panel). Bottom panels: PG 2304+042 (left panel), PKS 0518-45 (right panel). The lines are the same as in Figure 15.

Table 4
Silicate Feature Strengths Measured from the IRS/*Spitzer* Spectrum

Name	λ_p (μm)	$\text{Si}_{10\mu\text{m}}$	λ_p (μm)	$\text{Si}_{18\mu\text{m}}$	λ_p	$\text{Si}_{10\mu\text{m}}$	λ_p	$\text{Si}_{18\mu\text{m}}$	Ref.
NGC 7213	10.7 ± 0.1	0.52 ± 0.05	17.3 ± 0.1	0.23 ± 0.04	10.1	0.6	17.9	0.16	1
3C321	9.8 ± 0.1	-0.9 ± 0.1	18.1 ± 0.1	-0.09 ± 0.05
3C405	9.8 ± 0.1	-0.73 ± 0.07	18.2 ± 0.1	-0.06 ± 0.04
3C33	9.7 ± 0.1	-0.17 ± 0.04	17.4 ± 0.1	0.12 ± 0.04
ESO434-G40	9.9 ± 0.1	-0.37 ± 0.03	17.8 ± 0.1	0.07 ± 0.02
III Zw2	10.4 ± 0.8	0.04 ± 0.05	16.6 ± 0.1	0.11 ± 0.03
IRAS 03450+0055	10.3 ± 0.1	0.15 ± 0.05	16.7 ± 0.1	0.08 ± 0.05
IRAS 05218-1212	9.2 ± 0.1	-0.06 ± 0.03	17.8 ± 0.1	0.13 ± 0.04
MCG-6-30-15	9.0 ± 0.1	-0.13 ± 0.03	17.3 ± 0.1	0.07 ± 0.04	10.2	0.02	18.3	0.10	1
MRK 1218	9.2 ± 0.1	-0.22 ± 0.1	16.5 ± 0.4	0.24 ± 0.07
Mrk 10	9.4 ± 0.1	-0.14 ± 0.05	17.4 ± 0.1	0.1 ± 0.06
Mrk 110	10.3 ± 0.1	0.19 ± 0.03	18.0 ± 0.1	0.25 ± 0.03
Mrk 176	11.6 ± 0.2	0.07 ± 0.03	17.3 ± 0.1	0.18 ± 0.04
Mrk 231	9.8 ± 0.1	-0.73 ± 0.02	17.3 ± 0.1	-0.18 ± 0.02	9.8	-0.62	17.9	-0.23	1
Mrk 3	9.8 ± 0.1	-0.45 ± 0.04	17.9 ± 0.1	0.19 ± 0.02
Mrk 348	9.4 ± 0.1	-0.29 ± 0.04	16.6 ± 0.1	0.18 ± 0.03
Mrk 463E	9.8 ± 0.1	-0.45 ± 0.02	18.0 ± 0.1	0.05 ± 0.03	9.8	-0.4	18.3	0.09	2
Mrk 50	10.8 ± 0.1	0.22 ± 0.08	17.9 ± 0.1	0.27 ± 0.26	10.8	0.24	18.3	0.37	3
Mrk 573	9.3 ± 0.1	-0.14 ± 0.03	17.3 ± 0.1	0.11 ± 0.02	9.4	-0.10	17.2	0.04	3
Mrk 734	10.7 ± 0.1	0.06 ± 0.04	18.0 ± 0.1	0.09 ± 0.04
Mrk 915	9.4 ± 0.1	-0.11 ± 0.07	17.3 ± 0.1	0.18 ± 0.05	10.4	0.05	17.1	0.27	3
NGC 3081	9.3 ± 0.1	-0.26 ± 0.03	17.3 ± 0.1	0.12 ± 0.06
NGC 7212	9.9 ± 0.1	-0.46 ± 0.09	17.3 ± 0.1	0.18 ± 0.04
NGC 788	9.4 ± 0.1	-0.25 ± 0.04	16.7 ± 0.1	0.14 ± 0.03	9.5	-0.08	20.5	0.02	3
PG 1149-110	11.6 ± 0.1	0.06 ± 0.05	17.3 ± 0.1	0.13 ± 0.03
PG 1244+026	10.9 ± 0.1	0.14 ± 0.06	17.3 ± 0.1	0.06 ± 0.04
PKS 2048-57	9.9 ± 0.1	-0.33 ± 0.02	15.3 ± 0.1	0.02 ± 0.02
TON 1542	10.9 ± 0.1	0.08 ± 0.06	17.8 ± 0.1	0.12 ± 0.03
UGC 3601	11.6 ± 0.1	0.1 ± 0.06	16.6 ± 0.1	0.20 ± 0.08
UM 614	10.9 ± 0.1	0.12 ± 0.05	17.6 ± 0.1	0.19 ± 0.1	10.7	0.17	17.2	0.16	3
B3-0754+394	10.1 ± 0.2	0.13 ± 0.09	17.7 ± 0.1	0.13 ± 0.17
F9	10.7 ± 0.1	0.13 ± 0.02	17.4 ± 0.1	0.13 ± 0.03

Table 4
(Continued)

Name	λ_p (μm)	Si ₁₀ μm	λ_p (μm)	Si ₁₈ μm	λ_p	Si ₁₀ μm	λ_p	Si ₁₈ μm	Ref.
IIZw136	9.2 ± 0.1	-0.06 ± 0.03	17.9 ± 0.1	0.09 ± 0.04
IZw1	9.7 ± 0.1	0.22 ± 0.03	17.8 ± 0.1	0.08 ± 0.03
PG 0007+106/Mrk 1501	11.6 ± 0.1	0.04 ± 0.05	16.3 ± 0.3	0.10 ± 0.03
PG 0923+129/Mrk705 ^a	9.2 ± 0.1	-0.09 ± 0.03	17.3 ± 0.1	0.16 ± 0.03
PG 1211+143	10.7 ± 0.1	0.23 ± 0.03	17.6 ± 0.1	0.15 ± 0.04
PG 1229+204/Mrk 771	9.2 ± 0.1	-0.15 ± 0.08	19.1 ± 0.2	0.07 ± 0.03
PG 1411+442	10.8 ± 0.1	0.17 ± 0.04	18.4 ± 0.2	0.1 ± 0.03
PG 1426+015/Mrk 1383	10.7 ± 0.1	0.17 ± 0.04	17.4 ± 0.1	0.15 ± 0.03
PG 1440+356/Mrk 478	9.3 ± 0.1	-0.09 ± 0.05	17.3 ± 0.1	0.07 ± 0.02
PG 1448+273	11.6 ± 0.1	0.08 ± 0.04	17.7 ± 0.1	0.14 ± 0.03
PG 1501+106/Mrk 841	9.4 ± 0.1	-0.09 ± 0.03	18.2 ± 0.1	0.14 ± 0.03
PG 1534+580/Mrk 290	10.7 ± 0.1	0.11 ± 0.03	17.9 ± 0.1	0.15 ± 0.03
ESO198-G24	9.9 ± 0.1	0.23 ± 0.05	16.3 ± 0.1	0.25 ± 0.06
ESO548-G81	10.7 ± 0.1	0.21 ± 0.04	16.8 ± 0.1	0.22 ± 0.04	10.7	0.31	18.0	0.17	3
NGC 2110	10.7 ± 0.1	^a 0.22 ± 0.03	16.5 ± 0.1	0.16 ± 0.02
Mrk 486/PG 1535+547	10.9 ± 0.1	0.17 ± 0.05	17.4 ± 0.1	0.10 ± 0.06
3C120 ^b	10.7 ± 0.1	0.19 ± 0.03	17.5 ± 0.1	0.13 ± 0.04	10.2	0.26	17.8	0.15	1
NGC 1275	10.6 ± 0.3	0.15 ± 0.02	17.9 ± 0.1	0.09 ± 0.03
NGC 7603	11.0 ± 0.1	0.21 ± 0.02	16.5 ± 0.1	0.17 ± 0.03	10.2	0.12	17.7	0.13	1
NGC 7603 ^c					11.7	0.16	17.1	0.13	3
MRK 1018	10.2 ± 0.1	0.23 ± 0.06	17.7 ± 0.1	0.16 ± 0.05
3C382	10.7 ± 0.1	0.24 ± 0.05	17.5 ± 0.1	0.20 ± 0.03
PG 1404+226	10.0 ± 0.1	0.24 ± 0.06	16.6 ± 0.1	0.2 ± 0.08
PG 2209+184 ^a	11.0 ± 0.1	0.25 ± 0.06	16.4 ± 0.1	0.21 ± 0.10
UGC 12282	Sy1.9	0.0169	42.8 [*]	10	9.2 ± 0.1	-0.31 ± 0.06	17.3 ± 0.1	0.15 ± 0.07	

Note. Columns 1 lists the name. Columns 2 and 3 list the wavelength where the 10 μm silicate emission feature peaks, and the 10 μm silicate strength. Columns 4 and 5 are like columns 2 and 3 but for the 18 μm silicate emission feature. Columns 6–9 are like columns 2–5 but for the values previously reported in the literature. Column 10 lists the reference. Ref.: (1): Thompson et al. (2009), (2): Sirocky et al. (2008), (3): Mendoza-Castrejón et al. (2015). ^aThe band 1 range from 8.0 to 8.5 μm . ^bThe band 1 range from 8.0 to 8.8 μm . ^cThe bands 1 and 2 range from 8.0 to 8.8 μm , and 14.0 to 14.5 μm , respectively.

Appendix C

Tables of Parameters

Here, we report the χ^2 and degree of freedom for each object in the Si–s sample fitted with the model combination: AGN, AGN+Stellar, AGN+H II, and AGN+Stellar+H II; see

Table 5. We also report the set of parameters obtained from the best fit (see Tables 6–10 and Figure 17), and the plots from modeling the nonstellar IRS/*Spitzer* spectrum of all objects in the Si–s sample. See Figures 18–26.

Table 5

All Fitting from Smooth Models of Fritz et al. (2006), Clumpy Models of Nenkova et al. (2008a, 2008b) and Hönig & Kishimoto (2010), and Disk+Outflow Models of Hönig & Kishimoto (2017)

Name	χ^2/dof					Name	χ^2/dof				
	C1	C2	C3	C4	Best		C1	C2	C3	C4	Best
NGC 7213						PG 2214+139					
Fritz+06	NM	NM	NM	NM	...	Fritz06	NM	187.3/123	NM	187.3/122	C2
Nenkova08	169.6/114	125.1/113	169.6/113	125.0/112	C2	Nenkova+08	NM	236.4/123	NM	236.4/122	C2
Hoenig10	NM	NM	NM	NM	...	Hoenig+10	NM	NM	NM	84.6/120	C4
Hoenig17	NM	NM	NM	NM	...	Hoenig+17	NM	NM	NM	22.9/117	C4
Stalevski16	NM	NM	NM	NM	...	Stalevski16	NM	181.6/120	NM	107.9/119	C4
PG 2304+042						PG 0804+761					
Fritz+06	NM	224.7/117	NM	224.7/116	C2	Fritz+06	124.0/125	77.9/124	124.0/124	77.9/123	C2
Nenkova+08	184.9/118	146.6/117	185.0/117	146.5/116	C2	Nenkova+08	NF	198.8/124	NF	190.2/123	C2
Hoenig+10	140/119	82.5/68	NM	75.9/117	C1	Hoenig+10	NM	NM	NM	222.5/124	C4
Hoenig+17	77.6/116	65.7/115	76.9/115	65.7/114	C2	Hoenig+17	89.0/123	89.0/122	59.6/122	59.6/121	C3
Stalevski16	NM	232.2/117	NM	NM	C2	Stalevski16	NM	137.5/124	NM	136.0/123	C2
PKS 0518-45						OQ208					
Fritz+06	NM	NM	NM	NM	...	Fritz+06	NM	NM	NM	NM	...
Nenkova+08	178/9118	150.8/117	178.9/117	151.0/116	C2	Nenkova+08	152.4/124	45.7/123	184.4/123	39.0/122	C4
Hoenig+10	87.4/119	59.7/118	87.4/118	54.0/117	C4	Hoenig+10	NM	NM	NM	NM	...
Hoenig+17	36.1/116	36.4/115	35.7/115	35.5/114	C1	Hoenig+17	NM	215.5/121	NM	211.1/120	C2
Stalevski16	194.8/118	191.1/117	196.4/117	191.1/116	C1	Stalevski16	NM	NM	NM	NM	...
PG 0844+349						NGC 4258					
Fritz+06	241.4/121	144.2/120	NM	144.2/119	C2	Fritz+06	NM	NM	NM	NM	...
Nenkova+08	162.5/121	37.9/120	162.5/120	37.4/119	C2	Nenkova+08	NM	122.4/110	82.8/110	85.0/109	C4
Hoenig+10	NM	57.7/121	NM	24.2/120	C4	Hoenig+10	NM	NM	NM	180.1/110	C4
Hoenig+17	29.2/119	27.1/118	20.3/118	14.9/117	C4	Hoenig+17	NM	NM	202.5/108	202.8/107	C3
Stalevski16	NM	97.2/120	NM	97.1/119	C2	Stalevski16	NM	NM	NM	NM	...
PG 1351+640						NGC 3998					
Fritz+06	NM	187.3/123	NM	187.3/122	C2	Fritz+06	NM	137.8/72	137.8/72	137.8/71	C2
Nenkova+08	NM	236.4/123	NM	236.4/122	C2	Nenkova+08	30.9/73	23.3/72	27.1/72	21.8/71	C2
Hoenig+10	NM	NM	NM	NM	...	Hoenig+10	29.5/74	27.2/73	28.8/73	28.7/72	C1
Hoenig+17	NM	NM	NM	NM	...	Hoenig+17	27.9/71	25.3/70	24.6/70	23.0/69	C1
Stalevski16	NM	NM	NM	NM	...	Stalevski16	NM	NM	NM	NM	...

Note. Column 1 lists the name and models. Columns 2–5 list the χ^2 and dof of each model combination: C1 indicates AGN model (torus or disk+outflow), C2 AGN +Stellar, C3 AGN+H II, and C4 AGN+Stellar+H II. Column 6 lists the combination of components that best fit the IRS/*Spitzer* spectrum. NM = Non-modeled, indicates that the spectrum is not fitted by this component or combination of components.

Table 6

Derived Parameters from Smooth Models of Fritz et al. (2006)

Name	Parameters						
	i (min;max) [0–90] deg	Θ (min;max) [20–60]	γ (min;max) [0–6]	β (min;max) [–1.0–0.0]	Y (min;max) [10–150]	τ (min;max) [0.3–10]	Covering Factor [0–1]
PG 2304+042	0.0*	20.0*	6.0*	–0.01*	10.0*	9.8 (9.1;10.0)	0.2*
PG 0844+349	12.9 (11.8;14.9)	20.0*	6.0*	–0.25 (–0.26;–0.20)	11.8 (11.6;12.0)	6.0 (5.9; 6.2)	0.1*
PG 1351+640	>84.5	<21.0	6.0*	–0.01*	35.9 (35.6;36.1)	7.4 (6.9; 7.6)	0.1*
PG 2214+139	70.0 (66.3; 71.6)	<22.1	0.0*	–0.5 (–0.6;–0.4)	10.4 (10.2; 10.7)	1.0 (0.9; 1.1)	0.6*
PG 0804+761	44.3 (34.1; 51.9)	<24	>5.7	–0.7 (–0.8;–0.7)	10.0*	3.0 (2.7; 3.2)	>0.1
NGC 3998	0.0*	<21	>5.9	–0.01*	>142	2.1 (2.1; 2.2)	0.1*

Note. Column 1 lists the name of the object modeled. Columns from 2 to 7 list the torus parameters that best reproduce the AGN-dominated IRS/*Spitzer* spectrum: the viewing angle i , the torus angular width σ deg, polar index γ and radial index β of the gas density distribution $\rho(r, \Theta) \propto r^\beta e^{-\gamma \times \cos(\Theta)}$ within the torus, the radial extend $Y = R_{\text{outer}}/R_{\text{inner}}$, and the optical depth $\tau_{9.7 \mu\text{m}}$. Column 7 lists the covering factor, which is derived using i , γ , and τ (see equation in González-Martín et al. 2019b). *Parameter unrestricted.

Table 7
Derived Parameters from Clumpy Models of Nenkova et al. (2008a, 2008b)

Name	Parameters						Covering Factor [0–1]
	i (min;max) [0–90] deg	N_0 (min,max) [1–15]	σ (min,max) [15–70] deg	Y (min;max) [5–100]	q (min,max) [0.0–2.5]	τ_V (min,max) [5–300]	
NGC 7213	0.01 (0.00; 1.47)	7.0 (6.1; 7.3)	<15.0	10.2 (10.0; 10.5)	<0.01	55.1 (51.6; 59.5)	<0.4
PG 2304+042	76.3 (74.0; 77.4)	13.1 (10.5; 13.6)	17.5 (15.0; 21.7)	10.0 (9.8; 10.1)	0.9 (0.6; 1.0)	10.0 (10.0; 10.3)	0.5 (0.4; 0.6)
PKS 0518–45	70.8 (69.0; 75.0)	12.8 (12.1; 14.1)	23.6 (20.7; 29.8)	10.0 (9.9; 10.0)	0.1 (0.0; 0.5)	10.0 (10.0; 10.6)	0.6 (0.6; 0.8)
PG 0844+349	78.3 (66.4; 90.0)	6.7 (4.2; 10.9)	20.3 (15.0; 41.0)	11.7 (10.5; 14.7)	0.5 (0.0; 1.2)	13.9 (10.0; 22.3)	0.5 (0.3; 0.9)
PG 1351+640	0.0*	7.6 (7.3; 10.4)	45.0 (44.3; 45.3)	30.3 (29.9; 31.0)	<0.01	15.5 (15.1; 15.9)	0.9*
PG 2214+139	>88.6	2.7 (2.1; 3.1)	24.7 (15.1; 39.7)	>91	>2.4	36.8 (33.2; 39.3)	>0.5
PG 0804+761	>76.9	1.0*	54.5 (27.0; 70.0)	100.0 (79.2; 100.0)	2.3*	87.8 (65.9; 100.9)	>0.5
OQ208	25.5 (0.0; 74.0)	1.3 (1.2; 3.4)	64.8 (24.4; 70.0)	11.7 (11.3; 13.5)	0.01 (0.00; 0.81)	>265.6	0.6 (0.3; 0.9)
NGC 4258	81.2 (72.8; 86.0)	1.5 (1.1; 1.8)	<20.4	7.8 (7.2; 8.6)	0.01 (0.00; 0.05)	>254.9	<0.3
NGC 3998	>87.5	1.7 (1.6; 1.8)	<36.4	100.0 (96.8; 100.0)	0.01 (0.00; 0.02)	20.1 (16.5; 24.3)	>0.5

Note. Column 1 lists the name of the object modeled. Columns from 2 to 7 list the torus parameters that best reproduce the AGN-dominated IRS/*Spitzer* spectrum: the viewing angle i , the number of clouds along the equatorial ray N_0 , the angular width σ deg, the radial extend Y , the index of the radial distribution of clouds q , and the optical depth τ_V . Column 7 lists the covering factor, which is derived using i , N_0 , and Θ (see equation in González-Martín et al. 2019b). *Parameter unrestricted.

Table 8
Derived Parameters from Clumpy Models of Hönig & Kishimoto (2010)

Name	Parameters					
	i (min;max) [0–90]	N_0 (min,max) [2.5–10.0]	θ (min,max) [50–60]	a (min,max) [–2.0–0.0]	τ_V (min;max) [30–80]	Covering Factor [0–1]
PG 2304+042	75.4 (49.6; 87.6)	<3.2	>55.0	–0.03 (–0.06; –0.01)	<32.7	>0.6
PKS 0518–45	51.8 (38.5; 55.8)	5.7 (3.1; 6.9)	58.5 (47.7; 60.0)	–0.01 (–0.06; –0.01)	45.9 (41.2; 63.8)	0.9 (0.8–1.0)
PG 0844+349	44.9 (0.0; 53.3)	3.1 (2.6; 4.2)	55.1 (46.2; 60.0)	–0.08 (–0.17; –0.03)	>73.9	0.8 (0.7–0.9)
PG 2214+139	30.0 (25.4; 33.3)	8.9 (8.0; 9.8)	56.7 (54.1; 59.5)	–1.1 (–1.2; –1.1)	>78.9	0.97 (0.95, 0.98)
PG 0804+761	29.9 (25.2; 30.4)	6.9 (6.4; 7.4)	>59.7	–0.7*	80.0 (79.3; 80.0)	>1.0
NGC 4258	31.0 (30.0; 32.2)	>9.7	>59.8	–0.01*	>79.6	1.0
NGC 3998	75.1 (59.1; 90.0)	2.9 (2.5; 3.6)	54.7 (32.7; 60.0)	–0.3 (–0.5; –0.2)	<43.8	0.8 (0.6; 0.9)

Note. Column 1 lists the name of the object modeled. Columns from 2 to 6 list the torus parameters that best reproduce the AGN-dominated IRS/*Spitzer* spectrum: the viewing angle i , the number of clouds along the equatorial ray N_0 , the angular width θ , the index of the radial distribution of clouds a , and the optical depth per cloud τ_V . Column 7 lists the covering factor which is derived using i , N_0 , and Θ (see equation in González-Martín et al. 2019b). *Parameter unrestricted.

Table 9
Derived Parameters from Disk+Outflow Models of Hönig & Kishimoto (2017)

Name	Parameters								Covering Factor [0–1]
	$i(\text{min,max})$ [0–90]	$N_0(\text{min,max})$ [5–10]	$a(\text{min,max})$ [–3.0–0.5]	$\Theta_w(\text{min,max})$ [7–15] deg	$\sigma_\theta(\text{min,max})$ [30–45] deg	$a_w(\text{min,max})$ [–2.5–0.5]	$h(\text{min,max})$ [0.1–0.5]	$f_{wd}(\text{min,max})$ [0.15–0.75]	
PG 2304+042	45.0 (44.1; 45.9)	<5.3	–2.5 (–2.7; –2.5)	10.4 (9.2; 11.2)	>44.6	–0.5*	>0.4	0.30 (0.30; 0.33)	>0.3
PKS 0518-45	29.6 (21.2; 33.9)	<6.1	–2.2 (–2.4; –2.0)	>9.0	38.8 (33.8; 43.0)	–0.5 (–0.9; –0.5)	0.12 (0.10; 0.16)	>0.41	>0.2
PG 0844+349	18.6 (0.1; 26.9)	>6.7	–2.0 (–2.3; –1.6)	>8.5	34.8 (33.5; 42.7)	–0.5 (–0.8; –0.5)	0.11 (0.10; 0.19)	0.73 (0.42; 0.75)	>0.2
PG 2214+139	15.6 (0.0; 16.8)	>6.6	–3.0 (–3.0; –2.8)	8.5 (7.0; 13.5)	>35.5	–0.5 (–0.9; –0.5)	0.4 (0.3; 0.5)	>0.40	>0.4
PG 0804+761	0.0*	>9.7	–2.4 (–2.4; –1.8)	10.3 (9.8; 10.8)	>44.3	–0.5*	0.18 (0.17; 0.20)	>0.73	>0.2
OQ208	0.0*	10.0*	–0.5*	9.9 (9.7; 10.1)	>44.9	–0.5 (–0.5; –0.5)	0.5*	0.75 (0.74; 0.75)	>0.4
NGC 4258	30.0 (25.6; 30.4)	>9.7	–2.1 (–2.1; –2.0)	7.1 (7.0; 7.5)	>44.5	–0.5 (–0.5; –0.5)	0.1*	>0.74	>0.1
NGC 3998	<26.31	<6.6	–0.5 (–1.1; –0.5)	12.7*	33.4 (31.0; 45.0)	–2.5 (–2.5; –1.5)	0.1*	>0.27	0.2*

Note. Column 1 lists the name of the object modeled. Columns from 2 to 9 list the disk and outflow parameters that best reproduce the AGN-dominated IRS/*Spitzer* spectrum: Disk: index of the radial distribution of clouds a , number of clouds along the equatorial ray N_0 , the scale height in the vertical Gaussian distribution of clouds h . Wind: index of the radial distribution of clouds in the wind a_w ; the half-opening angle of the wind Θ_w , and its angular width σ_θ . The viewing angle i and the ratio between the number of clouds along the cone and N_0 , f_{wd} . Column 7 lists the covering factor which is derived using the i , N_0 , Θ_w and, σ_θ (see equation in González-Martín et al. 2019b). *Parameter unrestricted.

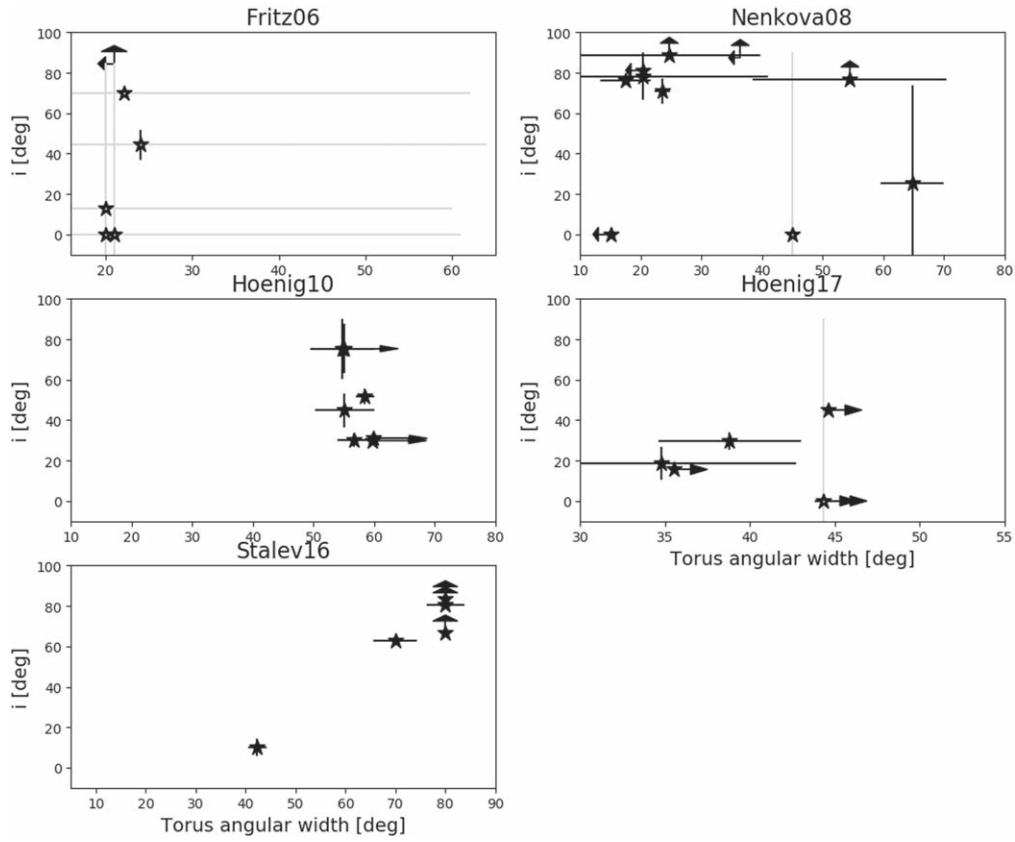


Figure 17. The viewing angle vs. the angular width derived from the Si-s sample for the smooth dusty torus of Fritz06, the clumpy torus models of Nenkova08 and Hoenig10, the disk+outflow torus model of Hoenig10, and the two-phase media models of Stalev16.

Table 10
Derived Parameters from Two-phase Media Models of Stalevski et al. (2016)

Parameters							
Name	$i(\text{min,max})$ [0–90]	$\sigma(\text{min,max})$ [10–80]	$p(\text{min,max})$ [0–1.5]	$q(\text{min,max})$ [0–1.5]	$Y(\text{min,max})$ [10–30]	$\tau_{9,7}(\text{min,max})$ [3–11]	Covering Factor [0–1]
PG 2304+042	>83.5	80.0 (60.0; 79.1)	0.01 (0.0; 0.02)	1.0 (1.0; 1.1)	10.0*	3.0 (0.1; 3.1)	>0.7
PKS 0518–45	>66.5	80.0 (60.0; 79.0)	0.01 (0.0; 0.01)	0.7 (0.6; 0.7)	10.0*	3.0 (0.1; 3.1)	>0.8
PG 0844+349	>80.5	80.0 (60.0; 76.2)	0.01 (0.0; 0.01)	1.5*	12.3 (11.9; 12.8)	3.1 (0.1; 3.3)	>0.6
PG 2214+139	63.0 (58.3; 64.9)	70.0 (67.8; 74.4)	>1.5	1.5*	<10.1	3.8 (3.6; 4.2)	0.7*
PG 0804+761	10.0 (0.0; 14.1)	42.3 (41.6; 44.1)	>1.5	1.5*	<10.2	10.8*	1.0*

Note. Column 1 lists the name of the object modeled. Column 2 lists the viewing angle i , column 2 lists the angular width σ of the torus. Columns 3 and 4 list the indices of the radial (p) and angular distribution (q) of the clouds. Column 5 gives the ratio between the outer and inner radius. Column 6 gives the optical depth $\tau_{9,7}$. Columns 7 list the covering factor. *Parameter unrestricted.

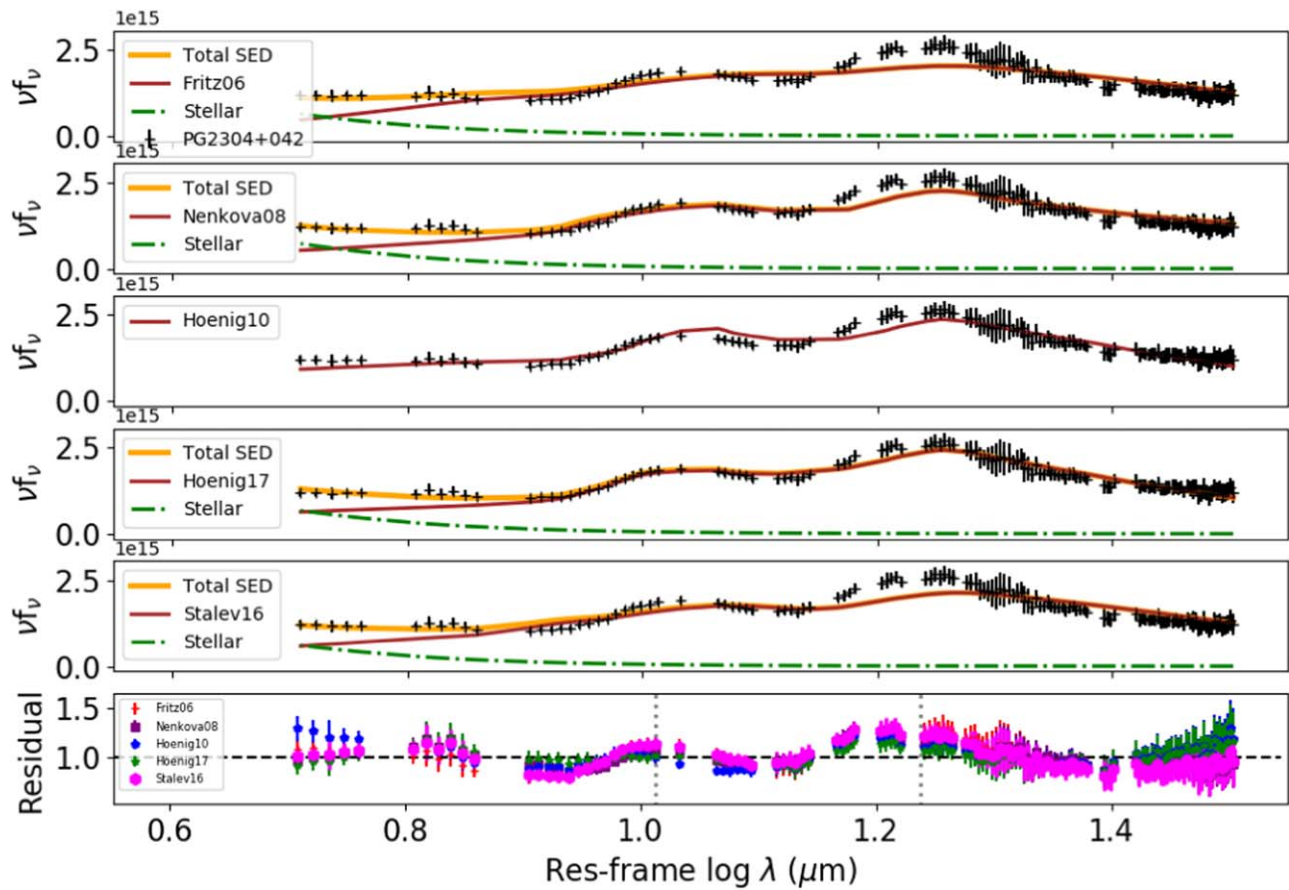


Figure 18. Modeling and residuals of the IRS/*Spitzer* spectrum of PG 2304+042. From top to bottom is the spectrum fitted assuming the [Fritz06](#) ($\chi^2_{\text{red}} \sim 1.20$), [Nenkova08](#) ($\chi^2_{\text{red}} \sim 0.32$), [Hoenig10](#) ($\chi^2_{\text{red}} \sim 0.20$), [Hoenig17](#) ($\chi^2_{\text{red}} \sim 0.13$), and [Stalevski16](#) ($\chi^2_{\text{red}} \sim 0.81$) models. The last panel shows the residuals defined as the ratio between the data and model. In all panels, the black points are the IRS/*Spitzer* spectrum and its error in ($\text{erg s}^{-1}\text{cm}^{-2}$), and the red solid line is the fitted torus model. The orange line is the total SED that results when more than one component, the stellar (green dotted–dashed line) and/or H II (blue dotted line), is added to model the spectrum.

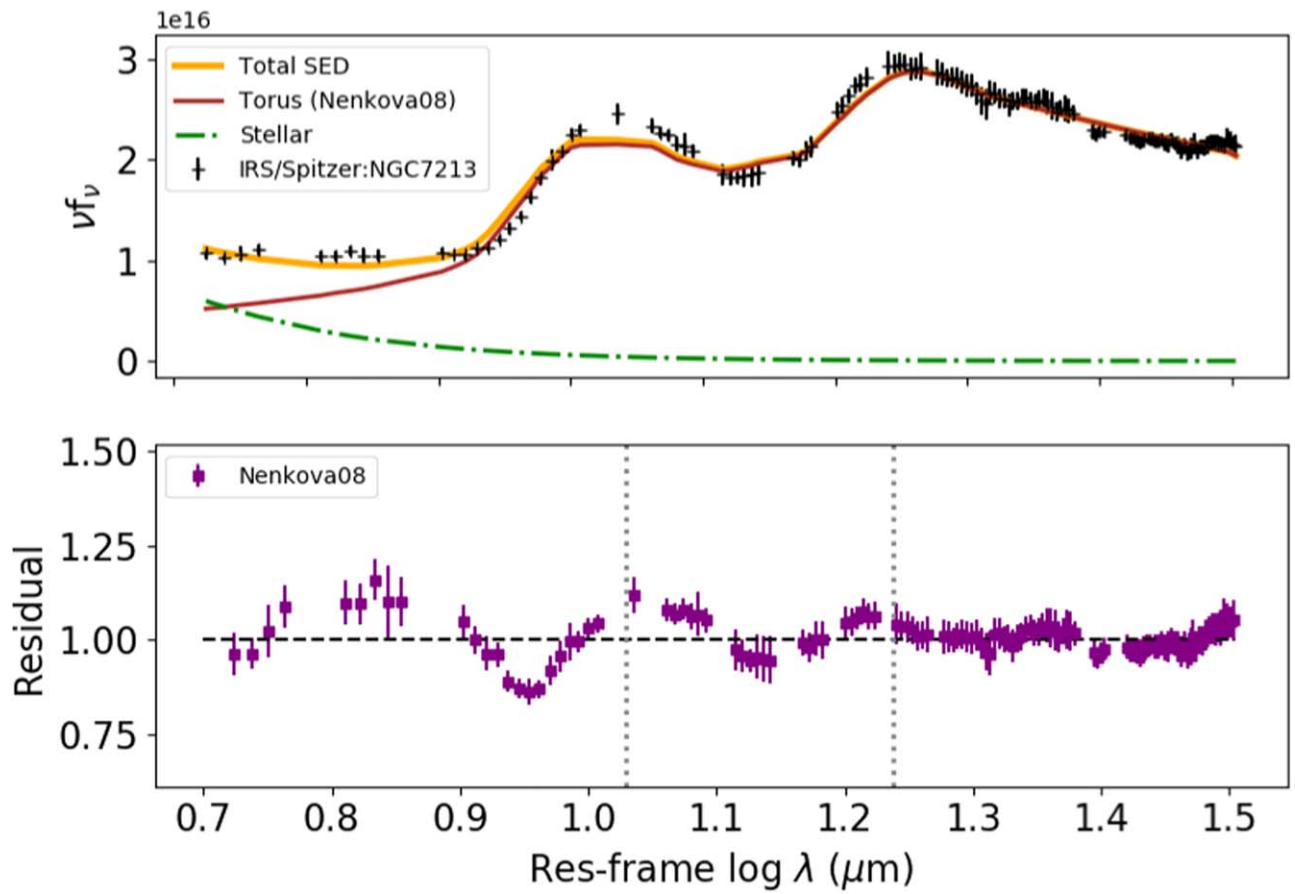


Figure 19. Modeling and residuals of the IRS/*Spitzer* spectrum of NGC 7213. The top panel shows the spectrum fitted assuming Nekova08 ($\chi^2_{\text{red}} \sim 1.11$). The bottom panel shows the residuals defined as the ratio between the data and models. In both panels, the black points are the IRS/*Spitzer* spectrum and its error in $\text{erg s}^{-1} \text{cm}^{-2}$, and the red solid line is the fitted torus model. The orange line is the total SED that results when more than one component, the stellar (green dotted-dashed line) and/or H II (blue dotted line), is added to model the spectrum.

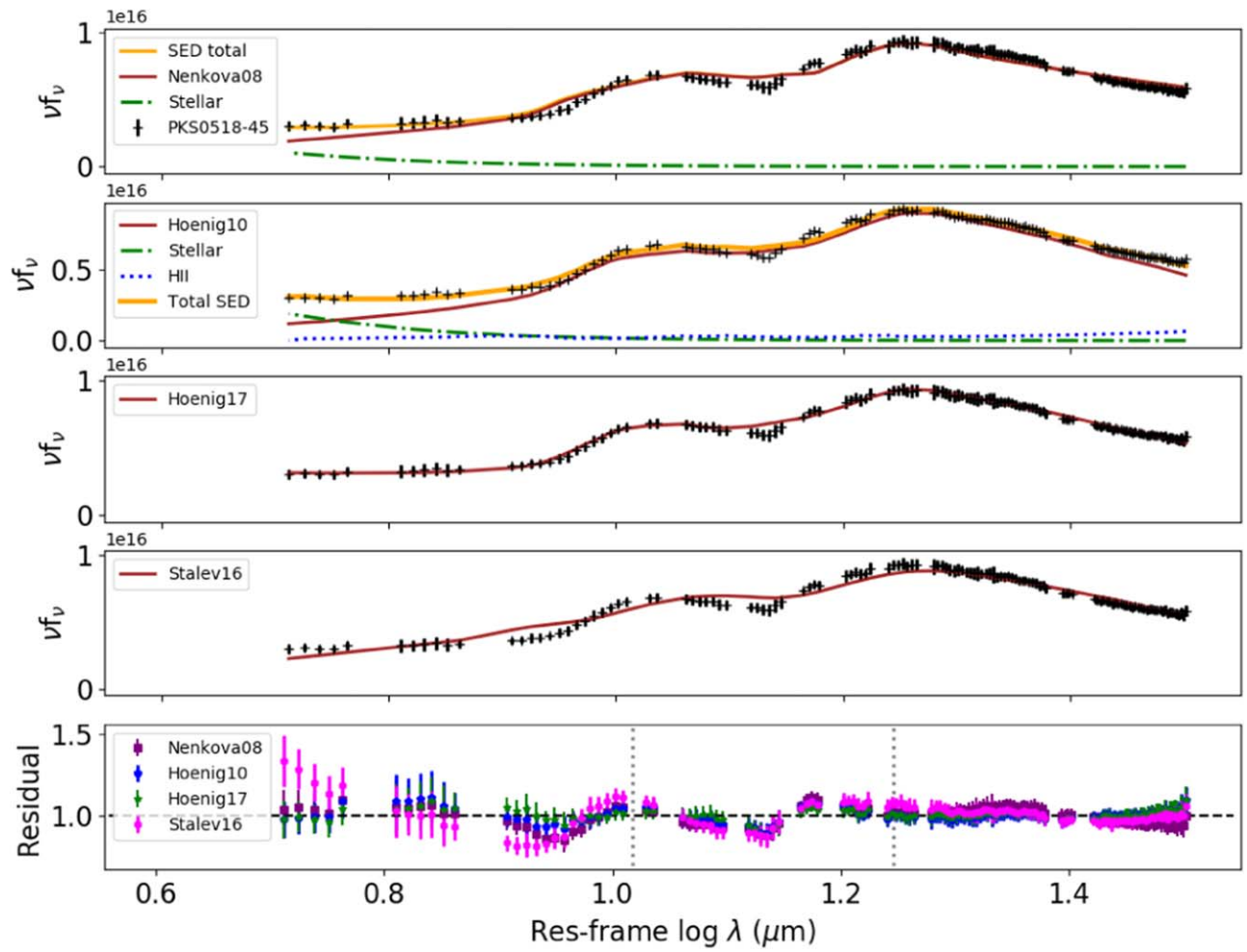


Figure 20. Modeling and residuals of the IRS/*Spitzer* spectrum of PKS 0518-45. From top to bottom, the panels show the spectrum fitted assuming the Nenkova08 ($\chi_{\text{red}}^2 \sim 1.29$), Hoenig10 ($\chi_{\text{red}}^2 \sim 0.46$), Hoenig17 ($\chi_{\text{red}}^2 \sim 0.31$), and Stalevski16 ($\chi_{\text{red}}^2 \sim 1.65$) models. The bottom panel shows the residuals defined as the ratio between the data and model. In all panels, the black points are the IRS/*Spitzer* spectrum and its error in $\text{erg s}^{-1}\text{cm}^{-2}$, and the red solid line is the fitted torus model. The orange line is the total SED that results when more than one component, the stellar (green dotted–dashed line) and/or H II (blue dotted line), is added to model the spectrum.

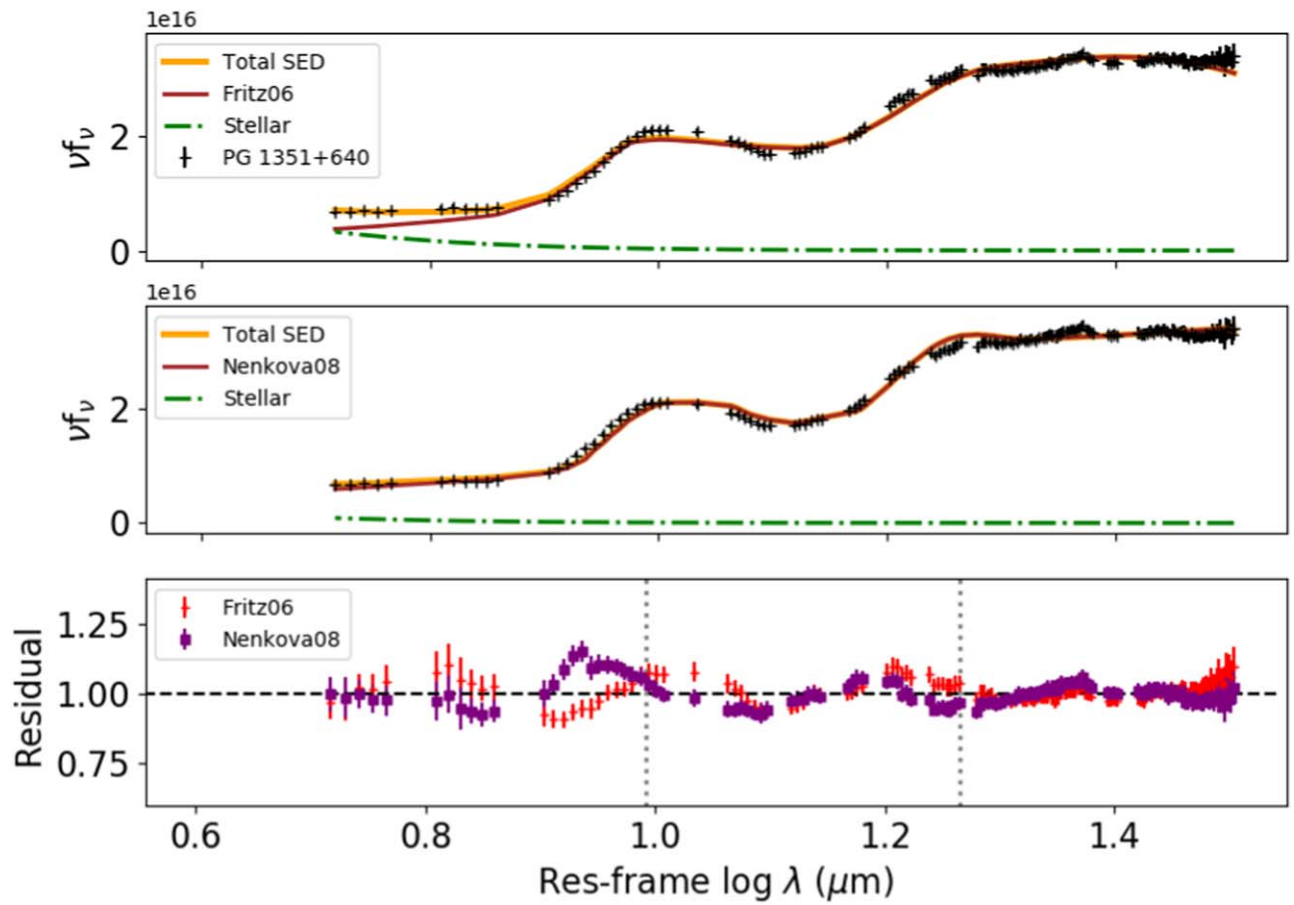


Figure 21. Modeling and residuals of the IRS/*Spitzer* spectrum of PG 1351+640. From top to bottom, the panels show the spectrum fitted assuming the [Fritz06](#) ($\chi^2_{\text{red}} \sim 1.52$) and [Nenkova08](#) ($\chi^2_{\text{red}} \sim 1.92$) models. The bottom panel shows the residuals defined as the ratio between the data and model. In all panels, the black points are the IRS/*Spitzer* spectrum and its error in $\text{erg s}^{-1}\text{cm}^{-2}$, and the red solid line is the fitted torus model. The orange line is the total SED that results when more than one component, the stellar (green dotted–dashed line) and/or H II (blue dotted line), is added to model the spectrum.

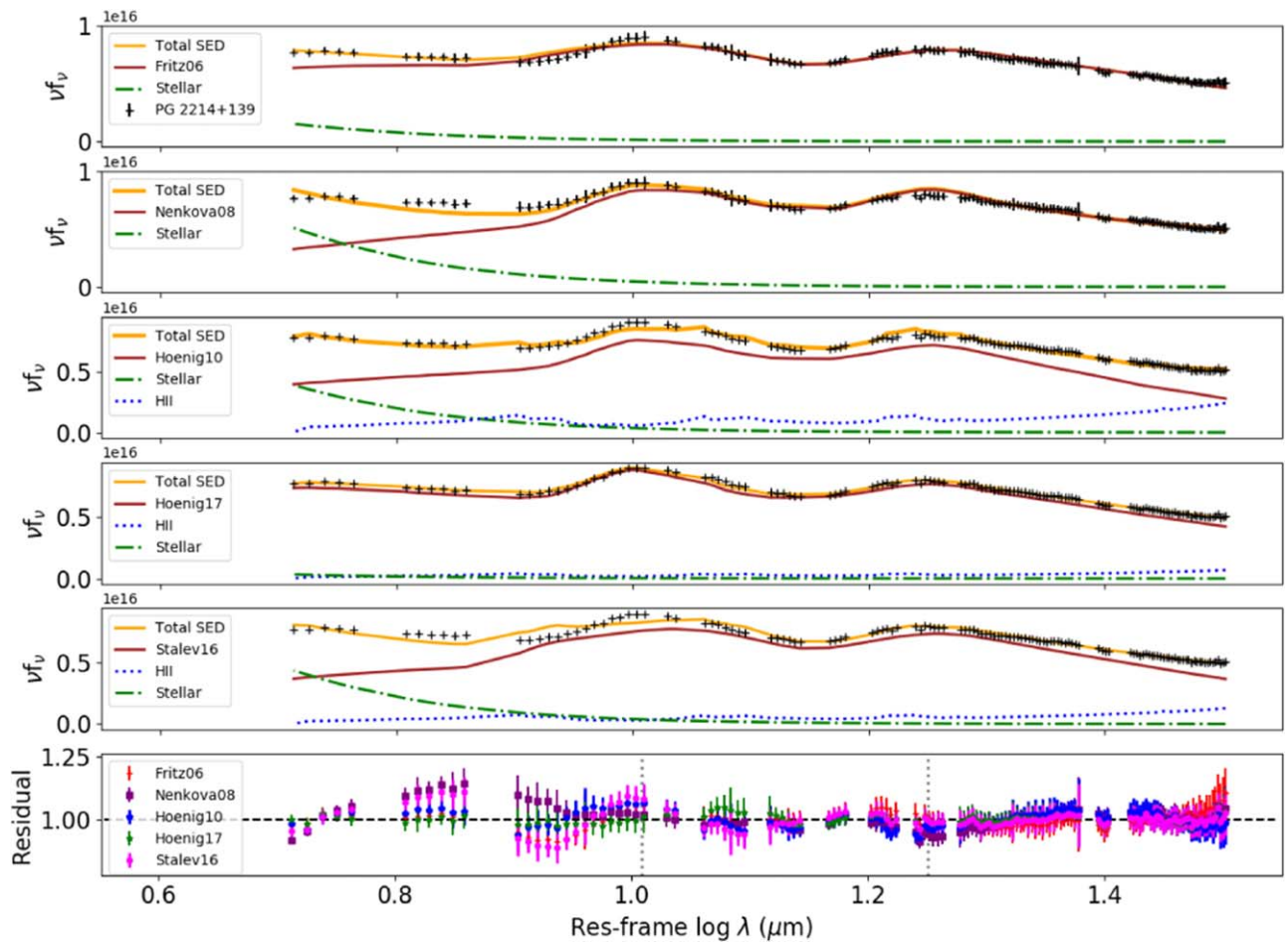


Figure 22. Modeling and residuals of the IRS/*Spitzer* spectrum of PG 2214+139. From top to bottom, the panels show the spectrum fitted assuming the [Fritz06](#) ($\chi^2_{\text{red}} \sim 1.52$), [Nenkova08](#) ($\chi^2_{\text{red}} \sim 1.92$), [Hoenig10](#) ($\chi^2_{\text{red}} \sim 0.71$), [Hoenig17](#) ($\chi^2_{\text{red}} \sim 0.20$), and [Stalevski16](#) ($\chi^2_{\text{red}} \sim 0.91$) models. The bottom panel shows the residuals defined as the ratio between the data and model. In all panels, the black points are the IRS/*Spitzer* spectrum and its error in $\text{erg s}^{-1} \text{cm}^{-2}$, and the red solid line is the fitted torus model. The orange line is the total SED that results when more than one component, the stellar (green dotted–dashed line) and/or H II (blue dotted line), is added to model the spectrum.

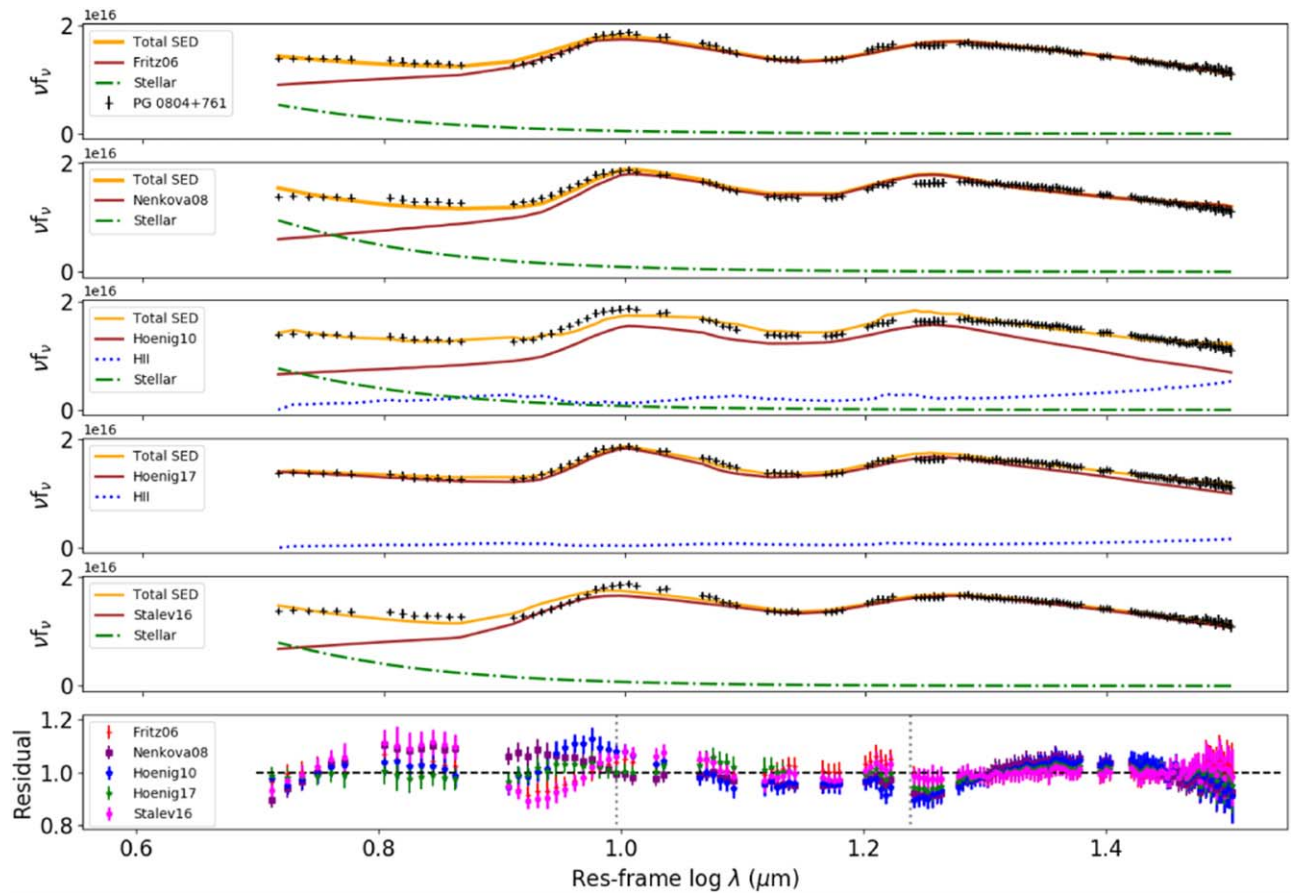


Figure 23. Modeling and residuals of the IRS/*Spitzer* spectrum of PG 0804+761. From top to bottom, the panels show the spectrum fitted assuming the [Fritz06](#) ($\chi^2_{\text{red}} \sim 0.63$), [Nenkova08](#) ($\chi^2_{\text{red}} \sim 1.60$), [Hoenig10](#) ($\chi^2_{\text{red}} \sim 1.79$), [Hoenig17](#) ($\chi^2_{\text{red}} \sim 0.49$), and [Stalevski16](#) ($\chi^2_{\text{red}} \sim 1.11$) models. The bottom panel shows the residuals defined as the ratio between the data and model. In all panels, the black points are the IRS/*Spitzer* spectrum and its error in $\text{erg s}^{-1} \text{cm}^{-2}$, and the red solid line is the fitted torus model. The orange line is the total SED that results when more than one component, the stellar (green dotted-dashed line) and/or H II (blue dotted line), is added to model the spectrum.

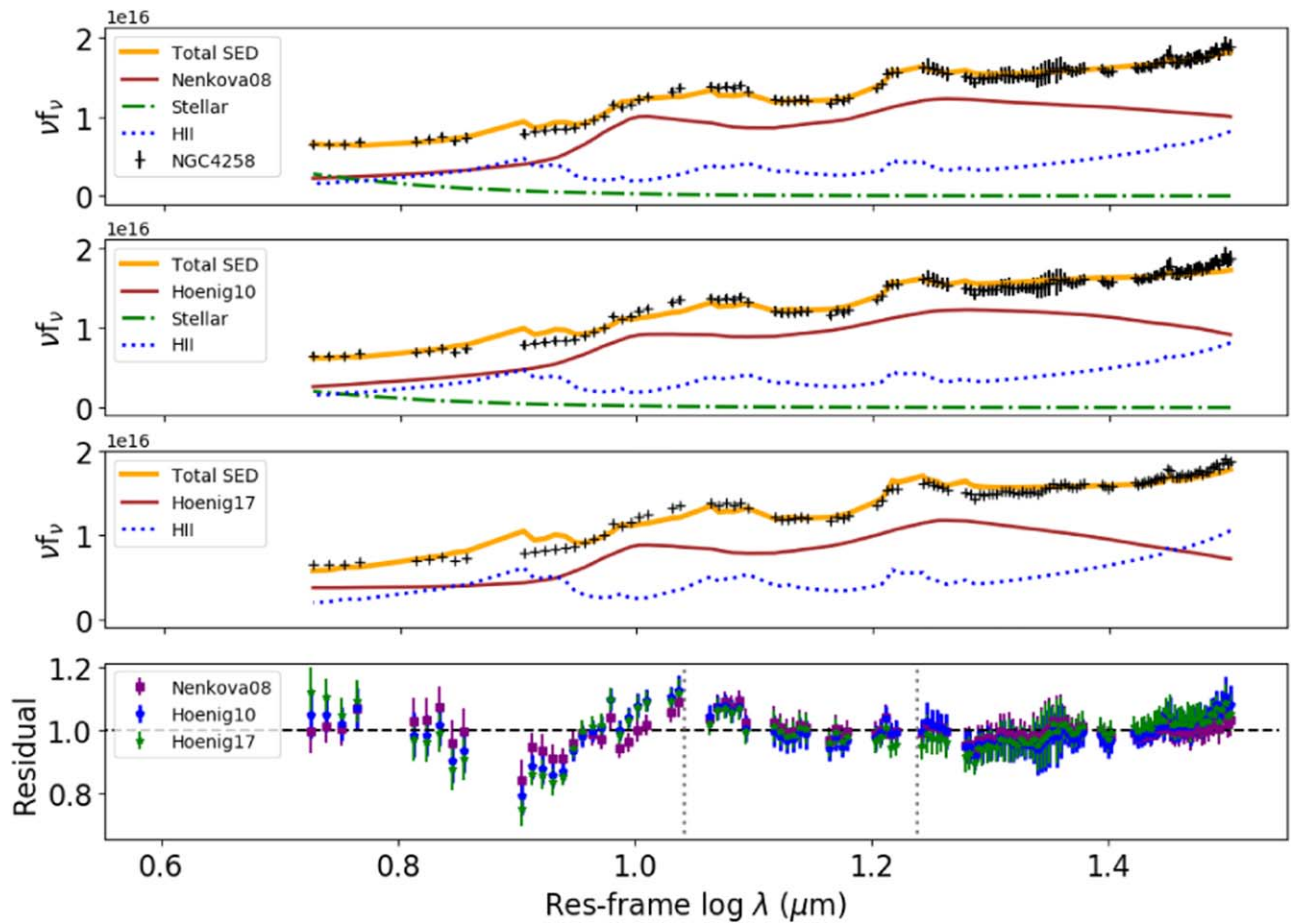


Figure 24. Modeling and residuals of the IRS/*Spitzer* spectrum of NGC 4258. From top to bottom, the panels show the spectrum fitted assuming the Nenkova08 ($\chi^2_{\text{red}} \sim 0.78$), Hoenig10 ($\chi^2_{\text{red}} \sim 1.64$), and Hoenig17 ($\chi^2_{\text{red}} \sim 1.88$) models. The bottom panel shows the residuals defined as the ratio between the data and model. In all panels, the black points are the IRS/*Spitzer* spectrum and its error in $\text{erg s}^{-1} \text{cm}^{-2}$, and the red solid line is the fitted torus model. The orange line is the total SED that results when more than one component, the stellar (green dotted–dashed line) and/or H II (blue dotted line), is added to model the spectrum.

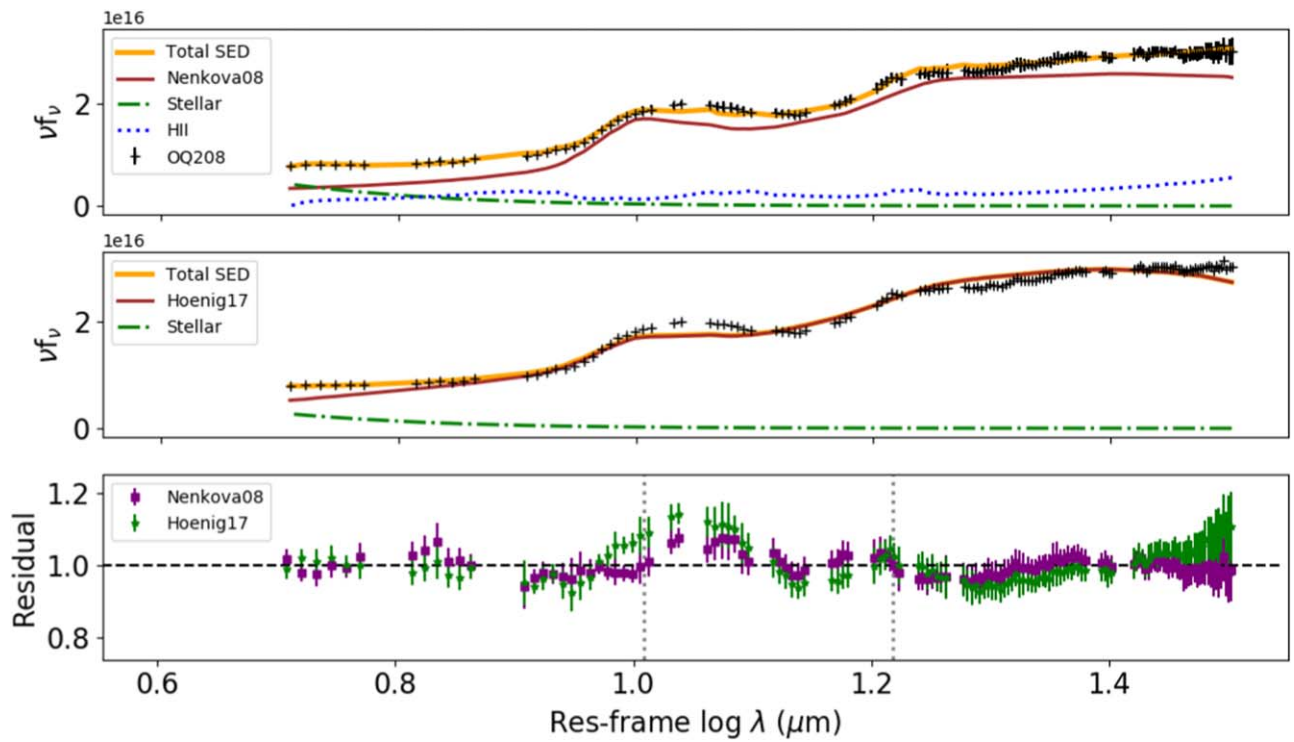


Figure 25. Modeling and residuals of the IRS/*Spitzer* spectrum of OQ208. From top to bottom, the panels show the spectrum fitted assuming the Nenkova08 ($\chi^2_{\text{red}} \sim 0.32$) and Hoenig17 ($\chi^2_{\text{red}} \sim 1.78$) models. The bottom panel shows the residuals defined as the ratio between the data and model. In all panels, the black points are the IRS/*Spitzer* spectrum and its error in $\text{erg s}^{-1}\text{cm}^{-2}$, and the red solid line is the fitted torus model. The orange line is the total SED that results when more than one component, the stellar (green dotted-dashed line) and/or H II (blue dotted line), is added to model the spectrum.

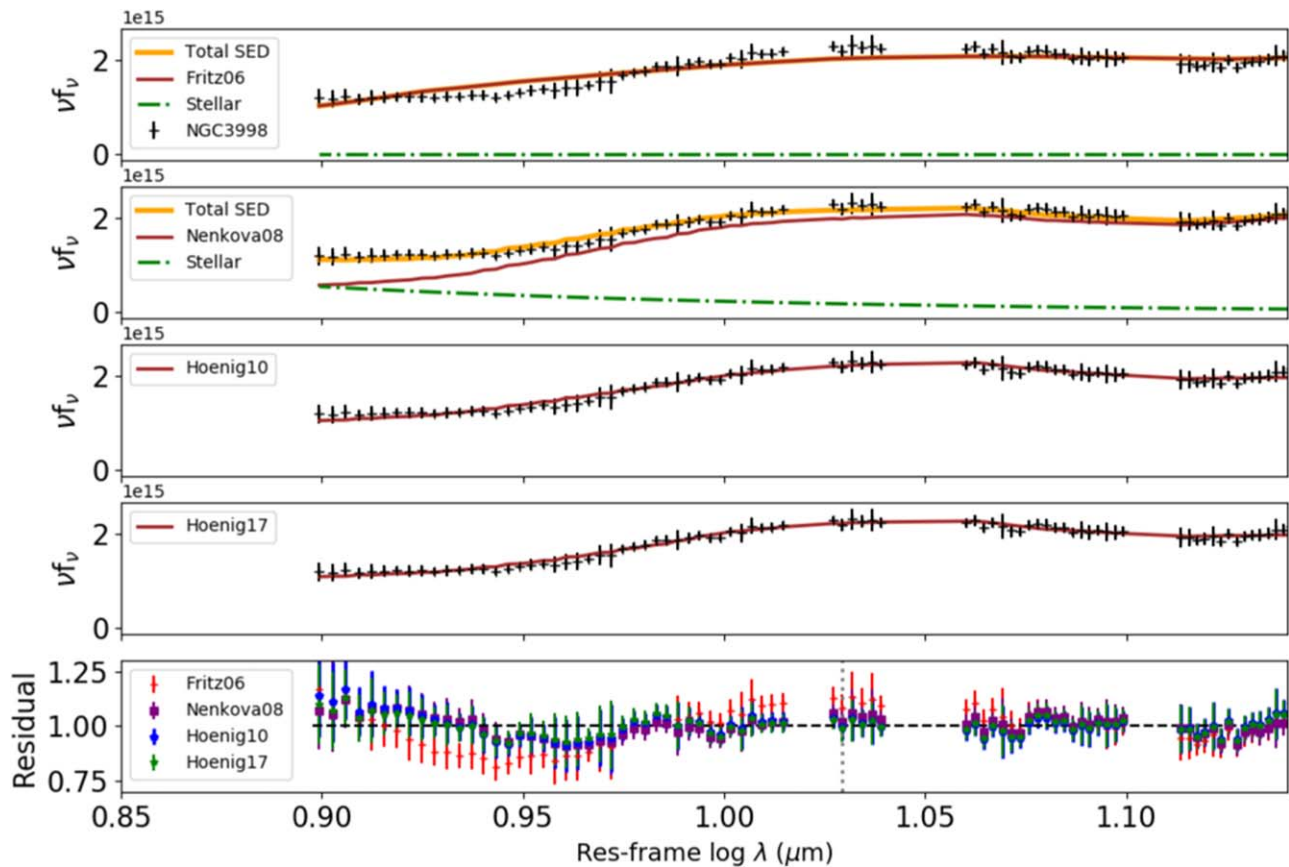


Figure 26. Modeling and residuals of the IRS/Spitzer spectrum of NGC 3998. From top to bottom, the panels show the spectrum fitted assuming the Fritz06 ($\chi^2_{\text{red}} \sim 1.91$), Nenkova08 ($\chi^2_{\text{red}} \sim 0.32$), Hoenig10 ($\chi^2_{\text{red}} \sim 0.40$), and Hoenig17 ($\chi^2_{\text{red}} \sim 0.39$) models. The last panel shows the residuals defined as the ratio between the data and model. In all panels, the black points are the IRS/Spitzer spectrum and its error in $\text{erg s}^{-1} \text{cm}^{-2}$, and the red solid line is the fitted torus model. The orange line is the total SED that results when more than one component, the stellar (green dotted-dashed line) and/or H II (blue dotted line), is added to model the spectrum.

ORCID iDs

M. Martínez-Paredes <https://orcid.org/0000-0002-0088-0103>
 O. González-Martín <https://orcid.org/0000-0002-2356-8358>
 T. Hoang <https://orcid.org/0000-0003-2017-0982>
 I. Aretxaga <https://orcid.org/0000-0002-6590-3994>

References

- Alexander, D. M., & Hickox, R. C. 2012, *NewAR*, 56, 93
 Alonso-Herrero, A., Ramos Almeida, C., Mason, R., et al. 2011, *ApJ*, 736, 82
 Antonucci, R. 1993, *ARA&A*, 31, 473
 Bianchi, S., Bonilla, N. F., Guainazzi, M., Matt, G., & Ponti, G. 2009, *A&A*, 501, 915
 Brightman, M., & Nandra, K. 2011, *MNRAS*, 413, 1206
 Bruzual, G., & Charlot, S. 2003, *MNRAS*, 344, 1000
 Buchanan, C. L., Gallimore, J. F., O’Dea, C. P., et al. 2006, *AJ*, 132, 401
 Cappi, M., Panessa, F., Bassani, L., et al. 2006, *A&A*, 446, 459
 Cusumano, G., La Parola, V., Segreto, A., et al. 2010, *A&A*, 510, A48
 Draine, B. T. 2003, *ApJ*, 598, 1026
 Draine, B. T., Dale, D. A., Bendo, G., et al. 2007, *ApJ*, 663, 866
 Dudik, R. P., Weingartner, J. C., Satyapal, S., et al. 2007, *ApJ*, 664, 71
 Dullemond, C. P., & van Bemmell, I. M. 2005, *A&A*, 436, 47
 Efsthathiou, A., & Rowan-Robinson, M. 1995, *MNRAS*, 273, 649
 Elvis, M., Wilkes, B. J., McDowell, J. C., et al. 1994, *ApJS*, 95, 1
 Feltre, A., Hatziminaoglou, E., Fritz, J., & Franceschini, A. 2012, *MNRAS*, 426, 120
 Fritz, J., Franceschini, A., & Hatziminaoglou, E. 2006, *MNRAS*, 366, 767
 García-González, J., Alonso-Herrero, A., Hönig, S. F., et al. 2017, *MNRAS*, 470, 2578
 González-Martín, O., Masegosa, J., García-Bernete, I., et al. 2019a, *ApJ*, 884, 10
 González-Martín, O., Masegosa, J., García-Bernete, I., et al. 2019b, *ApJ*, 884, 11
 González-Martín, O., Masegosa, J., Hernán-Caballero, A., et al. 2017, *ApJ*, 841, 37
 Granato, G. L., Danese, L., & Franceschini, A. 1997, *MmSAI*, 68, 39
 Hao, L., Spoon, H. W. W., Sloan, G. C., et al. 2005, *ApJL*, 625, L75
 Hao, L., Weedman, D. W., Spoon, H. W. W., et al. 2007, *ApJL*, 655, L77
 Hatziminaoglou, E., Hernán-Caballero, A., Feltre, A., et al. 2015, *ApJ*, 803, 110
 Henning, T. 2010, *ARA&A*, 48, 21
 Hernán-Caballero, A., Alonso-Herrero, A., Hatziminaoglou, E., et al. 2015, *ApJ*, 803, 109
 Hernán-Caballero, A., Hatziminaoglou, E., Alonso-Herrero, A., et al. 2017, *FrASS*, 4, 30
 Hönig, S. F., & Kishimoto, M. 2010, *A&A*, 523, A27
 Hönig, S. F., & Kishimoto, M. 2017, *ApJL*, 838, L20
 Hönig, S. F., Kishimoto, M., Antonucci, R., et al. 2012, *ApJ*, 755, 149
 Hönig, S. F., Kishimoto, M., Gandhi, P., et al. 2010, *A&A*, 515, A23
 Hönig, S. F., Kishimoto, M., Tristram, K. R. W., et al. 2013, *ApJ*, 771, 87
 Houck, J. R., Roellig, T. L., Van Cleve, J., et al. 2004, *Proc. SPIE*, 5487, 62
 Ichikawa, K., Packham, C., Ramos Almeida, C., et al. 2015, *ApJ*, 803, 57
 Kemper, F., Vriend, W. J., & Tielens, A. G. G. M. 2005, *ApJ*, 633, 534
 Kishimoto, M., Hönig, S. F., Beckert, T., et al. 2007, *A&A*, 476, 713
 Krolik, J. H., & Begelman, M. C. 1988, *ApJ*, 329, 702
 Laor, A., & Draine, B. T. 1993, *ApJ*, 402, 441
 Lebouteiller, V., Barry, D. J., Spoon, H. W. W., et al. 2011, *ApJS*, 196, 8
 Li, A., & Draine, B. T. 2001, *ApJ*, 554, 778
 Li, M. P., Shi, Q. J., & Li, A. 2008, *MNRAS*, 391, L49
 López-Gonzaga, N., & Jaffe, W. 2016, *A&A*, 591, A128

- Lyu, J., Hao, L., & Li, A. 2014, *ApJL*, **792**, L9
- Lyu, J., Rieke, G. H., & Shi, Y. 2017, *ApJ*, **835**, 257
- Marconi, A., Risaliti, G., Gilli, R., et al. 2004, *MNRAS*, **351**, 169
- Martínez-Paredes, M., Alonso-Herrero, A., Aretxaga, I., et al. 2015, *MNRAS*, **454**, 3577
- Martínez-Paredes, M., Aretxaga, I., Alonso-Herrero, A., et al. 2017, *MNRAS*, **468**, 2
- Mason, R. E., Lopez-Rodriguez, E., Packham, C., et al. 2012, *AJ*, **144**, 11
- Mason, R. E., Ramos Almeida, C., Levenson, N. A., Nemmen, R., & Alonso-Herrero, A. 2013, *ApJ*, **777**, 164
- Mateos, S., Carrera, F. J., Alonso-Herrero, A., et al. 2016, *ApJ*, **819**, 166
- Mathis, J. S., Rumpl, W., & Nordsieck, K. H. 1977, *ApJ*, **217**, 425
- Mendoza-Castrejón, S., Dultzin, D., Krongold, Y., et al. 2015, *MNRAS*, **447**, 2437
- Minezaki, T., Yoshii, Y., Kobayashi, Y., et al. 2004, *ApJL*, **600**, L35
- Mor, R., Netzer, H., & Elitzur, M. 2009, *ApJ*, **705**, 298
- Neškova, M., Ivezić, Ž., & Elitzur, M. 2002, *ApJL*, **570**, L9
- Neškova, M., Sirocky, M. M., Ivezić, Ž., & Elitzur, M. 2008a, *ApJ*, **685**, 147
- Neškova, M., Sirocky, M. M., Nikutta, R., Ivezić, Ž., & Elitzur, M. 2008b, *ApJ*, **685**, 160
- Neugebauer, G., Oke, J. B., Becklin, E. E., & Matthews, K. 1979, *ApJ*, **230**, 79
- Nikutta, R., Elitzur, M., & Lacy, M. 2009, *ApJ*, **707**, 1550
- Ossenkopf, V., Henning, T., & Mathis, J. S. 1992, *A&A*, **261**, 567
- Pei, Y. C. 1992, *ApJ*, **395**, 130
- Peterson, B. M. 1997, in IAU Coll. 159: Emission Lines in Active Galaxies: New Methods and Techniques 113 (San Francisco, CA: ASP), 489
- Pier, E. A., & Krolik, J. H. 1992, *ApJ*, **401**, 99
- Raban, D., Jaffe, W., Röttgering, H., et al. 2009, *MNRAS*, **394**, 1325
- Ramos Almeida, C., Alonso-Herrero, A., Esquej, P., et al. 2014, *MNRAS*, **445**, 1130
- Ramos Almeida, C., Levenson, N. A., Alonso-Herrero, A., et al. 2011, *ApJ*, **731**, 92
- Ramos Almeida, C., & Ricci, C. 2017, *NatAs*, **1**, 679
- Riffel, R. A., Storchi-Bergmann, T., & McGregor, P. J. 2009, *ApJ*, **698**, 1767
- Robson, I., Dunlop, J., Taylor, G., & Hughes, D. 1995, *BAAS*, **27**, 1415
- Sambruna, R. M., Tombesi, F., Reeves, J. N., et al. 2011, *ApJ*, **734**, 105
- Sanders, D. B., Phinney, E. S., Neugebauer, G., Soifer, B. T., & Matthews, K. 1989, *ApJ*, **347**, 29
- Schinnerer, E., Eckart, A., & Tacconi, L. J. 1998, *ApJ*, **500**, 147
- Schweitzer, M., Groves, B., Netzer, H., et al. 2008, *ApJ*, **679**, 101
- Shi, Y., Rieke, G. H., Hines, D. C., et al. 2006, *ApJ*, **653**, 127
- Siebenmorgen, R., Haas, M., Krügel, E., & Schulz, B. 2005, *A&A*, **436**, L5
- Sirocky, M. M., Levenson, N. A., Elitzur, M., Spoon, H. W. W., & Armus, L. 2008, *ApJ*, **678**, 729
- Smith, J. D. T., Draine, B. T., Dale, D. A., et al. 2007, *ApJ*, **656**, 770
- Srinivasan, S., Kemper, F., Zhou, Y., et al. 2017, *P&SS*, **149**, 56
- Stalevski, M., Fritz, J., Baes, M., et al. 2012, *MNRAS*, **420**, 2756
- Stalevski, M., Ricci, C., Ueda, Y., et al. 2016, *MNRAS*, **458**, 2288
- Sturm, E., Hasinger, G., Lehmann, I., et al. 2006, *ApJ*, **642**, 81
- Sturm, E., Schweitzer, M., Lutz, D., et al. 2005, *ApJL*, **629**, L21
- Suganuma, M., Yoshii, Y., Kobayashi, Y., et al. 2006, *ApJ*, **639**, 46
- Thompson, G. D., Levenson, N. A., Uddin, S. A., et al. 2009, *ApJ*, **697**, 182
- Tristram, K. R. W., Burtscher, L., Jaffe, W., et al. 2014, *A&A*, **563**, A82
- Tueller, J., Baumgartner, W. H., Markwardt, C. B., et al. 2010, *ApJS*, **186**, 378
- Ueda, Y., Ishisaki, Takahashi, T., Makishima, K., & Ohashi, T. 2005, *ApJS*, **161**, 185
- Véron-Cetty, M.-P., & Véron, P. 2010, *A&A*, **518**, A10
- Wada, K. 2012, *ApJ*, **758**, 66
- Wada, K., Papadopoulos, P. P., & Spaans, M. 2009, *ApJ*, **702**, 63
- Werner, M. W., Roellig, T. L., Low, F. J., et al. 2004, *ApJS*, **154**, 1
- Winter, L. M., Veilleux, S., McKernan, B., & Kallman, T. R. 2012, *ApJ*, **745**, 107
- Xie, Y., Li, A., & Hao, L. 2017, *ApJS*, **228**, 6
- Younes, G., Porquet, D., Sabra, B., & Reeves, J. N. 2011, *A&A*, **530**, A149
- Zhou, X.-L., & Zhang, S.-N. 2010, *ApJL*, **713**, L11